Abstract

Engineering of Geometrically Organized Blood Vessels for Quantitative Assays on a Microfluidic Chip

Hyunjae Lee

School of Mechanical and Aerospace Engineering

The Graduate School

Seoul National University

This thesis describes two microfluidic platforms that generate geometrically optimized microvessels for establishing various vascular biology related models. For vascular permeability assay, a novel microfluidic design was developed to form multiple perfusable 3D microvessels. The microvessels were formed by a natural angiogenic process and exhibit reliable functional barrier properties. The vessels acquired barrier function similar to those measured *in vivo* experiments with relatively low permeability coefficients for *in vitro* measurements. Manipulation of

barrier properties by addition of agonists and growth factors, and the modeling of cancer microvessels were also demonstrated.

For cancer angiogenesis and intravasation assay, a novel microfluidic design was developed to form a perfusable 3D microvessel with empty perivascular region, induced by natural vasculogenic process. For cancer angiogenesis assay, U87MG cancer cell line was introduced at the perivascular region. The cancer sprouts were observed three days after the cancer introduction, and could be attenuated by the treatment of anti-VEGF, bevacizumab. For cancer intravasation assay, MDA-MB-231 cancer cell line was introduced into the perivascular region and their migration toward the vessel wall was observed. Treatment of TNF-α showed disrupted morphology of the vessel junctions and increased portion of the intravasated cancer cells, agreeing with the previous *in vivo* studies.

The models have potential to be applied for various studies, including cancer cell or leukocyte extravasation, mechanotransduction of endothelial cells to the intraluminal flow. The robustness and reproducibility of these microfluidic chip-based microvessels, combined with the feasibility for flexible customizable chip design, promise to make it a versatile device for future investigations in fundamental vascular biology as well as drug screening.

Keywords: Microfluidic; Angiogenesis; Vascular permeability; Perfusable microvessel; Metastasis; Tissue Engineering

Student Number: 2012-30735

Contents

I	**INTRODUCTION** ·····	1
1	Capillary in a human body ·····	1
1.1	Introduction of the capillary ·····	1
1.2	Barrier function of the capillary ·····	1
1.3	Capillary in the cancer progression ·····	3
2	*In vitro* capillary models ·····	3
2.1	Conventional models for the capillary ·····	4
2.2	Microfluidic-based models for the capillary ·····	5
2.2.1	Attaching ECs to the walls of hydrogel channels	6
2.2.2	Utilizing the angiogenic/vasculogenic properties of endothelial cells·····	13
2.3	Limitations of the previous microfluidic-based capillary models ·····	18
2.4	Motivation and objectives·····	20

II DEVELOPMENT OF A MICROFLUIDIC PLATFORM FOR HIGH-THROUGHPUT VASCULAR PERMEABILITY ASSAY…… 22

1 Advantage of this platform…… 22

2 Materials and methods…… 22

2.1 Cell culture…… 22

2.2 Microfluidic chip fabrication…… 23

2.3 Hydrogel and cell loading…… 23

2.4 Microscopy…… 24

2.5 Immunostaining…… 25

2.6 Permeability factor treatments…… 25

2.7 Anti-VEGF neutralization…… 26

2.8 Permeability coefficient measurement…… 26

3 Results…… 29

3.1 Schematic of the microfluidic chip…… 29

3.2 HUVEC sprouting across vessel channel induced by LF…… 37

3.3	Formation of tight junctions observed with immunostained junctional proteins……	44
3.4	Vascular permeability measurement……	48
3.5	Microvessel induced by U87MG and their permeability response to bevacizumab treatment……	54
4	Discussion……	61
III	**DEVELOPMENT OF A MICROFLUIDIC PLATFORM FOR CANCER METASTASIS AND ANGIOGENESIS ASSAY**……	69
1	Advantage of this platform……	69
2	Materials and Methods……	70
2.1	Cell culture, immunostaining, and reagents……	70
2.2	Microfluidic device fabrication……	71
2.3	Hydrogel and cell loading into the metastasis chip….	73
2.4	Microscopy……	73
2.5	Data analysis……	74

3	Results……	75
3.1	Metastasis chip design……	75
3.2	Formation of perfusable microvessels with smooth and continuous boundaries……	81
3.3	Characterization of the microvessel……	86
3.4	Cancer angiogenesis assay……	92
3.5	Cancer intravsation assay……	98
4	Discussion……	104
IV	**CONCLUSION**……	108
Bibliography ……		110

List of Figures

Figure 1.1 Schematic of microvessel construction by using silicon housing and microneedles as molds ····· 8

Figure 1.2 Construction of a microvessel network using a micropatterned silicon stamp as a mold ····· 10

Figure 1.3 A three-dimensional (3D) microvessel network formed by rapid casting of carbohydrate glass with a 3D printer····· 12

Figure 1.4 An array of microvessels formed inside the microfluidic chip by utilizing the angiogenic properties of ECs····· 15

Figure 1.5 A microvascular network formed by utilizing the vasculogenic or angiogenic process of HUVECs····· 17

Figure 2.1 Schematic of the microfluidic chip for microvessel engineering····· 31

Figure 2.2 Computational simulation of the gel filling inside the vessel channel····· 34

Figure 2.3 Micrograph of the gel and cell loading into the microfluidic chip····· 36

Figure 2.4 The experimental setup for inducing microvessel with LF····· 38

Figure 2.5 Day by day image of the microvessel growth in the chip 40

Figure 2.6 HUVEC sprout inducing without LFs····· 43

Figure 2.7 Immunostaining for ZO-1 (tight junction protein) with three dimensional stacking····· 45

Figure 2.8 Fluorescence imaging of junctional proteins····· 47

Figure 2.9 Vascular permeability measurement with fluorescence micrographs of vessel filled with FITC-dextran····· 49

Figure 2.10 Quantification of the permeability responses····· 52

Figure 2.11 The experimental setup for inducing microvessel with U87MG····· 55

Figure 2.12 HUVEC sprout growth induced by U87MG····· 56

Figure 2.13 Permeability of the microvessels induced by U87MG and the bevacizumab treatment····· 58

Figure 2.14 Permeability imaging of the microvessel induced by U87MG····· 59

Figure 2.15 Junctional imaging of the microvessel induced by U87MG····· 60

Figure 2.16 Subordinate conditions for determining dimensions of PDMS structures in the vessel channel ····· 66

Figure 2.17 Comparison between this platform and the conventional Transwell assay ····· 68

Figure 3.1 Entire schematic drawing and detailed dimensions of the chip····· 72
Figure 3.2 Top-down view of the metastasis chip design scheme and experimental procedures····· 79
Figure 3.3 HUVEC concentration optimization for generating smooth and continuous vessel boundary····· 83
Figure 3.4 Time-lapse micrograph of the microvessel formation in $6 X 10^6$ /ml HUVEC concentration····· 85
Figure 3.5 Geometric characterization of the fully developed microvessel····· 87
Figure 3.6 DIC Micrograph of the microvessel wall and fluorescence micrograph of the same region with the introduction of 20 kDa FITC-dextran into the lumen····· 89
Figure 3.7 Junctional images of microvessel in day 7····· 91
Figure 3.8 Comparison of the microvessel wall before and three days in control experiment, and the cancer injection with bevacizumab treatment····· 94
Figure 3.9 Comparison of the microvessel wall before and three days after the cancer injection····· 95
Figure 3.10 Quantification of coverage area and numbers of sprouts·· 97
Figure 3.11 Micrographs of a cancer cell trans-migrating through the microvessel wall····· 99

Figure 3.12 Micrograph of the cancer intravasation····· 101

Figure 3.13 Micrograph of the VE-Cadherin expressed at the cell-to-cell junction in the microvessel····· 103

I. INTRODUCTION

1. Microvessels in a human body

1.1 Introduction of the Microvessels

Microvessels refer to the smallest systems of blood vessels in a living system, including arterioles, venules, metarterioles and capillaries. Blood capillaries connect arterioles and venules with complex vascular network, and compose the infrastructure of the body by covering the entire region in a living system. Their diameter is about 20~40 μm, and composed of a monolayer of endothelial cells covered with pericytes. Pericytes are contractile cells that embedded on the basement membrane around the endothelial cells, and play crucial role in the stabilization of the capillaries and regulation of the blood flow at the capillary level. During the embryological development, capillaries are formed through vasculogenesis, which is a *de novo* production that differentiates endothelial cells into vascular tube network. More vascular branches are formed from the vascular tube network and start to cover the entire body, which is called angiogenesis.

1.2 Barrier function of the microvessels

The blood circulatory system is a highly efficient system that maintains life by delivering nutrients and oxygen to every cell in the tissue. Blood constantly

circulates and selectively delivers essential factors while taking away waste products. At the center of this efficient system, selective barrier properties are exhibited by the endothelial cells lining the capillaries. The barrier function of capillaries can modulate context-specific and tissue-specific demands of oxygen, nutrients as well as mediate cellular (i.e. immune cells) traffic across blood stream and the tissue. Additionally, functional barriers are important in maintaining homeostasis and physiological functions of diverse organs. Although capillary barrier function has some degree of plasticity to maintain homeostasis, its abnormalities can cause various pathological states. Tumor progression starts from the excessive angiogenesis from the pre-existing blood vessels to the cancer colony. Abnormal increase of the vascular permeability near the cancer site can help the cancer angiogenesis, by the excessive extravasation of the plasma protein toward the cancer site, forming a provisional matrix for the migration of the endothelial cells. Abnormally increased vascular permeability can also cause chronic inflammation [1, 2], capillary leak syndrome [3] and pulmonary fibrosis [4] can lead to further progression of those pathological states. Thus misregulated vascular hyperpermeability is a potential therapeutic target for intervention. Better understanding of biological properties and mechanism of vascular permeability will lead to more effective treatment targets and result in new types of drugs.

1.3 Microvessels in the cancer progression

Cancer cells constantly interact with surrounding capillaries during different stages of metastasis [5, 6]. Cancer angiogenesis happens when the colonies grow and begin to secrete factors that stimulate surrounding capillaries to grow towards the colony. The new capillaries supply increasing amount of nutrients and oxygen to growing tumors which further recruit more capillaries. Cancer cells from the colonies start to penetrate through the surrounding tissue and blood vessels, circulate in the blood, and enter secondary sites in the perivascular region then grow to establish secondary colonies [7]. Therefore, angiogenesis and penetration of cancer cells through the capillaries (transendothelial migration) have been investigated extensively as they are the main steps for the progression of cancer metastasis. However, it has been difficult to realistically mimic the multiple steps of cancer metastasis *in vitro* due to difficulty in establishing physiological blood vessel models and spatially well-defined co-cultures of cancer and ECs. Therefore, an *in vitro* model that can mimic the metastatic cascade in a well-controlled microenvironment with more realistic blood vessel model is needed for further understanding metastasis.

2. *In vitro* microvessel models

2.1 Conventional models for the microvessels

Numerous *in vivo* and *in vitro* models have been developed to model capillaries [8]. Although animal models offer an ideal experimental platform, they require great amount of labor, time, and cost [9-11]. Furthermore, variability in animals and other factors make it difficult to isolate different effects and perform controlled experiments with statistical confidence. Therefore, *in vitro* models have been developed and used in order to overcome the limitations of the *in vivo* models. Most of the *in vitro* models developed to date are based on 2D endothelial monolayers cultured on permeable membranes. Typically, vascular permeability has been measured by introducing fluorescent molecules from either apical or basal region and measuring fluorescence intensity on the opposite side after a given time [12-16], transendothelial electrical resistance measurements [17-19], or immunohistochemistry or Western blotting of junctional protein expression (i.e. ZO-1 or occludin) [20, 21].

In transwell assay, cancer cells are grown in the lower chamber, and the upper chamber is cultured with endothelial cells in an extracellular matrix like collagen or Matrigel for modeling cancer angiogenesis. Tube formation [22] or migration of the endothelial cells [23] can be observed in response to the cancer-derived factors. For modeling the transendothelial migration of cancer cells, endothelial cells are cultured to confluence on a Petri dish or porous

membrane, and the penetration of the cancer cells through the endothelial monolayer can be observed following several hours to days of incubation [24-29]. Although these models partly represent blood vessel characteristics, lack of three-dimensionality and incompatibility with media perfusion have limited their validity as tools for modeling blood vessels.

2.2 Microfluidic-based models for the microvessels

Two-dimensional monolayer models have several limitations. They poorly represent the structural characteristics of the body, as they replicate only a portion of the blood vessel wall without any circular or lumenized (hollowed) structures. Additionally, 2D monolayer models cannot be used to study luminal flow with 3D tubular microvessel structures; thus, replicating the effect of physiological blood flow and the interactions with other cell types remains challenging.

To overcome these disadvantages, much effort has been devoted to recreating 3D structural characteristics of capillaries *in vitro* by utilizing microfabrication approaches. Soft lithography and polydimethylsiloxane (PDMS)-based microfluidic devices have opened a new era of *in vitro* models for biological research [30]. The use of these microchips has several advantages over conventional macroscale platform-based *in vitro* models [31].

Substrates with micro-nano patterns or microstructures that mimic the *in vivo* cellular microenvironment can be incorporated *in vitro*. Additionally, complex environmental factors can be precisely integrated and controlled, such as chemical gradients or interstitial flow that provides an *in vivo*-like environment. As a microchip uses a much smaller volume of reagent and the number of cells compared to conventional models, performing biological research using a microchip also lowers research costs. The microfluidic capillary models are grouped into two main types [32]: (1) Attaching ECs to the wall of a micropatterned hydrogel structure, and (2) using natural morphogenic processes for capillary formation inside a microfluidic device by spatially controlling the patterning of the hydrogel.

2.2.1 Attaching ECs to the walls of hydrogel channels

This scheme uses micropatterned hydrogels and ECs that attach to the wall to create capillaries on a chip. Chrobak et al. created a lumenized microvessel by constructing a collagen gel with a long, hollow structure using a silicon housing and a microneedle (Fig. 1.1) [33]. The microneedle-containing silicone housing is filled with collagen, and the microneedle is removed after collagen polymerization to leave a hollow microchannel structure. By attaching a confluent culture of ECs onto the wall of the hollow collagen structure, a 3D capillary that has tubular structure was engineered *in vitro*.

Vascular permeability was investigated using this microvessel, and the interaction between ECs and other cell types such as leukocytes or pericytes was examined by perfusion of media inside the capillary lumen.

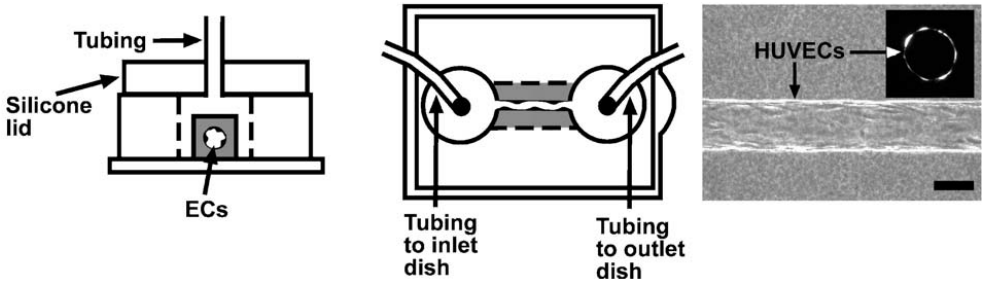

Figure 1.1 Schematic of microvessel construction by using silicon housing and microneedles as molds. Endothelial cells (ECs) were attached to the hydrogel wall to form a microvessel structure. Micrograph on right side shows top and sectioned view (inset) of the formed microvessel. Scale bar, 100 μm. (Chrobak et al., 2006)

Bischel et al. developed a simpler technique to generate hollow structures inside a hydrogel using “viscous finger patterning.” [34]. During polymerization of a hydrogel inside the microchannel, the partially polymerized hydrogel in the central part of the channel is washed away by passive pumping-based media flow [35], leaving a hollow lumen-like structure inside the hydrogel. ECs are attached inside the wall of the hollow structure to complete the capillaries with a 3D tubular structure on the chip. Multiple, parallel capillaries are created to observe angiogenesis toward a vascular endothelial growth factor (VEGF) gradient as well as the effect of smooth muscle cells on the angiogenic process. Consequently, this device can be used for various angiogenesis assays using different growth factors and drug candidates.

Zheng et al. replicated a network of capillaries rather than a single tube (Fig. 1.2) [36]. The microvascular structure was patterned on a collagen Type I gel using a microstructured silicone stamp. First, the patterned collagen is housed between two flex-glass pieces, followed by attaching ECs to the collagen wall. Several aspects of vascular biology were observed, such as interactions between pericytes and ECs, endothelial barrier function under different media conditions or co-cultured cells, and interactions between whole blood components and endothelium under a perfused flow condition.

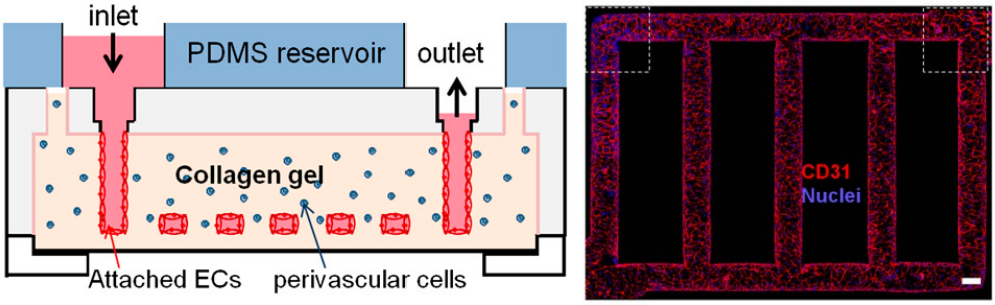

Figure 1.2 Construction of a microvessel network using a micropatterned silicon stamp as a mold. The micropatterned hydrogel was coated with ECs to model the microvessel network. The micrograph of the sample immunostained with CD31 shows robust microvessel network formation. Scale bar, 100 μm. (Zheng *et al.*, 2012)

Miller et al. established a novel method of creating a capillary network in a hydrogel structure (Fig. 1.3) [37]. Pertinent levels of carbohydrate glass—formed by mixing sucrose, glucose, and dextran in water and boiling off the solvent—were extruded to model capillaries by optimizing the nozzle velocity and diameter of a 3D printer. After thermally extruding the carbohydrate glass network utilizing the 3D printer, a fibrin gel was used to cover the capillaries, similar to interstitial ECM. The carbohydrate glass is dissolved with cell media, leaving the network structure inside the fibrin. ECs are attached to the fibrin gel walls to form a capillary network in the tissue. The fibrin gel can be encapsulated with fibroblasts and co-cultured with ECs to form a robust capillary network. The researchers clearly showed that hepatocytes (liver cells) in the gel exhibit increased metabolic functions by establishing a microvascular structure inside the hydrogel.

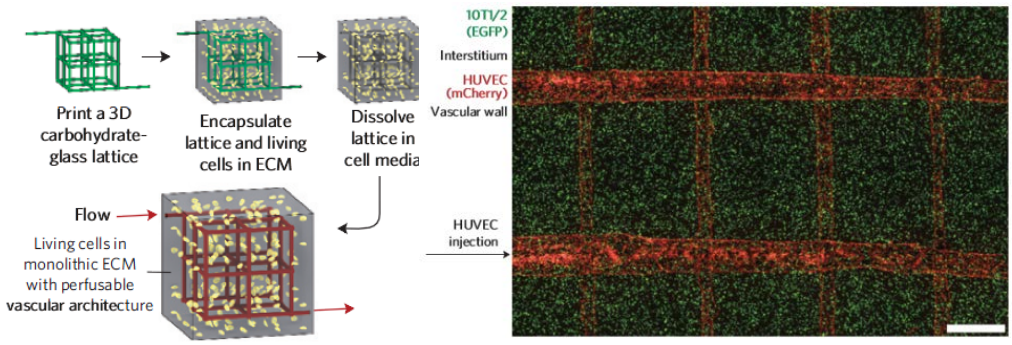

Figure 1.3 A three-dimensional (3D) microvessel network formed by rapid casting of carbohydrate glass with a 3D printer. The lattice of the carbohydrate glass was covered with a perivascular cell-containing hydrogel and melted with cell media to form the hollowed network inside the hydrogel tissue. The micrograph (right) shows HUVECs expressing mCherry (red fluorescent protein) that are attached to the hydrogel wall to generate the microvessel network. 10T1/2 cells (mouse fibroblast cell line) expressing EGFP (green fluorescent marker) are embedded with hydrogel to visualize interstitium. Scale bar, 1 mm. (Miller *et al.*, 2012)

2.2.2 Utilizing the angiogenic/vasculogenic properties of endothelial cells

Numerous studies in vascular biology have shown that ECs have morphogenic features that differentiate into a lumenized capillary structure by stimulation with several growth factors (e.g., VEGF and basic fibroblast growth factor [bFGF]) [38] or by co-culture with other cell types such as fi broblasts in ECM-like hydrogels, including collagen and fibrin [39]. Naturally lumenized capillaries can be engineered on a chip by combining the angiogenic/vasculogenic properties of ECs with construction of microstructures.

Raghavan et al. introduced a method that geometrically controls the shape of capillaries formed by the vasculogenic process [40]. A mixture of collagen gel and ECs was added to micropatterned PDMS channels, and the cells were stimulated with bFGF and VEGF to promote vasculogenesis. The capillaries formed by the ECs were geometrically aligned in various shapes by the geometrical confinement of the PDMS. Various shapes and radial sizes of capillaries could be achieved by modifying the collagen concentration and design of the PDMS microchannels. Although media perfusion in these capillaries is not possible because external pumps or other pumping systems cannot be connected to a defined capillary inlet or outlet, this dimensionally confining method for engineering various capillary shapes has the potential for use in many tissue engineering applications.

Yeon et al. established an array of perfusable capillaries on a single microfluidic chip (Fig. 1.4) [41]. After the fibrin gel was selectively patterned in the middle of a PDMS channel array as a provisional matrix for angiogenic sprouts, ECs were attached to both sides of the fibrin gel wall. The ECs were stimulated to form sprouts by co-culture with fibroblasts. After 3–4 days, the endothelial sprouts from both sides of the middle channel connected to form lumenized perfusable capillaries. Various dimensions or networks of capillaries can be engineered by fabricating different PDMS geometries.

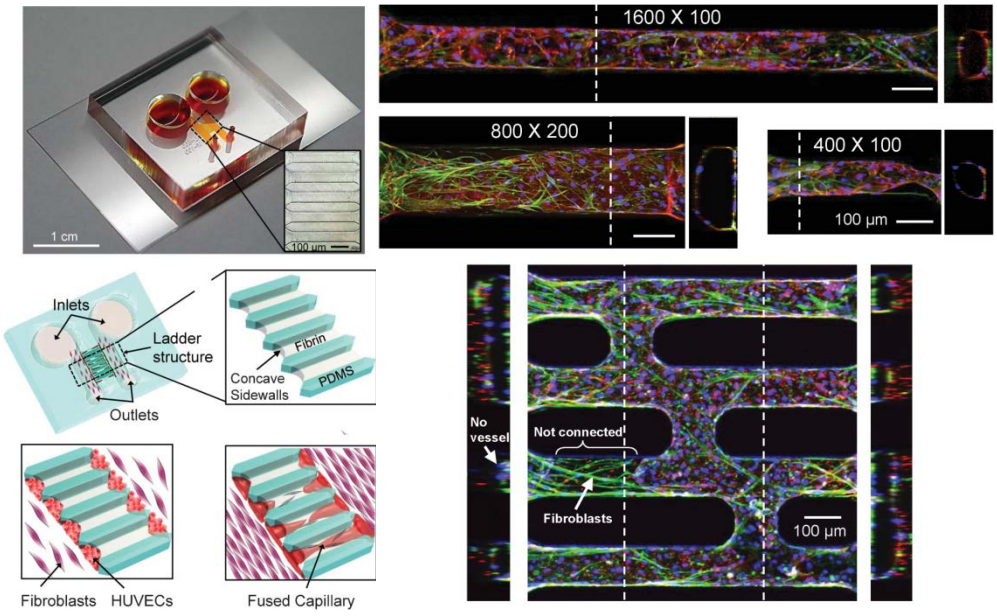

Figure 1.4 An array of microvessels formed inside the microfluidic chip by utilizing the angiogenic properties of ECs (top left). HUVECs were attached on both sides of the fibrin gel patterned inside the microchannel (bottom left). HUVECs were co-cultured with lung fibroblasts to stimulate the angiogenic process. The HUVEC sprouts from both sides were fused to form perfusable microvessels. Various shapes and network of the microvessel were formed by controlling the geometry of the microchannel (top and bottom right). Cross-sectional views at the dotted lines are shown next to respective micrographs. (Yeon *et al.*, 2012)

Kim et al. used two approaches to generate a perfusable capillary network [42]: filling the middle channel with a fibrin gel and EC mixture for the vasculogenic process, and filling the middle channel with fibrin gel and attaching ECs on the gel wall for the angiogenic process (Fig. 1.5). Fibroblasts were co-cultured, and ECs were stimulated to form a capillary network by the secreted factors of the fibroblasts. After the perfusable capillary network is formed in 4–5 days, various aspects of vascular biology were investigated, including vascular permeability, alignment of F-actin, expression of EC nitric oxide by stimulation from media perfusion, and interactions with other cell types, such as pericytes and immune cells.

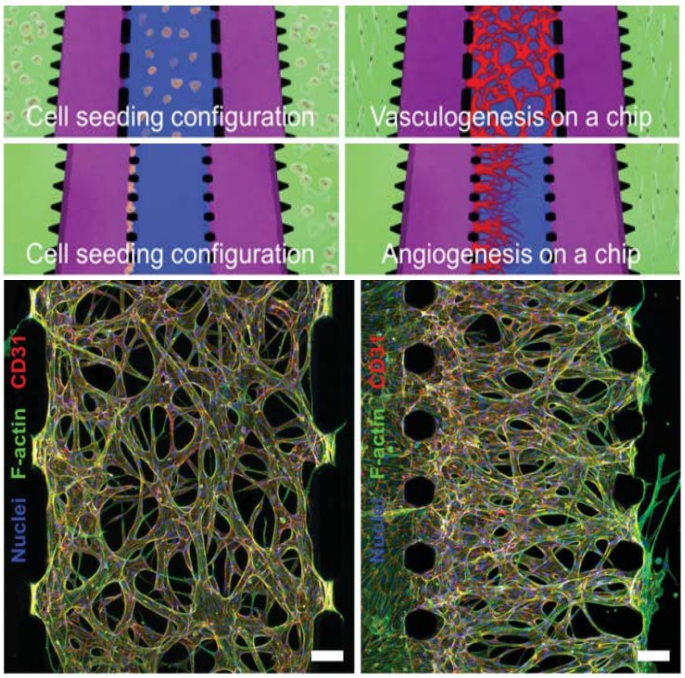

Figure 1.5 A microvascular network formed by utilizing the vasculogenic or angiogenic process (upper and lower part of schematic, respectively) of HUVECs. HUVECs were either encapsulated in or attached to the fibrin gel (blue channels) and co-cultured with lung fi broblasts (green channels) to stimulate microvessel formation. The microvessel network was opened to both media channels (purple channels) for perfusion by media. Immuno-fluorescent images show the engineered microvessel network formed by the vasculogenic and angiogenic (left and right in micrographs, respectively) process. Scale bars, 100 μm. (Kim *et al.*, 2013)

Hsu et al. demonstrated another microfluidic system in which an array of vascular networks was engineered [43]. Based on an analogy between an electrical circuit and a microfluidic network, this system applied a physiological level of media flow into EC/fibroblast co-cultured microvessel chambers. ECs were mixed with fibroblasts in the fibrin gel to stimulate the vasculogenic process, and interstitial flow by a pressure drop across the vessel chamber applied a physiological level of interstitial flow, mimicking the in vivo microenvironment.

2.3 Limitations of the previous microfluidic-based microvessel models

The microvessel models that attach ECs to the walls of hydrogel channels share several features. They commonly use molds and housings to construct the hydrogel structure, which resemble the luminal structure of capillaries, followed by attaching EC monolayers to the walls of the structure to recreate capillaries. Although these *in vitro* capillaries have properties similar to the Transwell membrane model, their structural properties are much closer to *in vivo* capillaries and can be easily perfused with cell culture media. An advantage of this method is that capillary geometry can be controlled easily through the use of micro fabricated mold structures according to the experimental purpose. Furthermore, as the shape of the mold determines capillary structure, applying physiological levels of media using an external

pump is easy, as the applied shear stress can be calculated from the engineered capillary diameter and pump flow rate. However, the capillaries developed in these models are not formed by a vasculogenic or angiogenic process, which is the main biological process that living organisms use to establish the circulatory system. That is, the physiological relevance of these engineered capillaries with actual *in vivo* blood vessels is attenuated, as the process for engineering the microvascular structure is based mainly on artificially depositing ECs on hydrogel walls.

In contrast to methods that attach ECs to hydrogel walls, the main advantage of the methods that utilizes the angiogenic/vasculogenic properties of ECs is that they are based on a more *in vivo*-like vessel formation process. Moreover, these schemes, particularly those for the vasculogenesis methods, can be applied to tissue engineering. As the degree of biological similarity between the capillaries produced using this scheme and the *in vivo* condition has not been fully realized, future work should concentrate on investigating the detailed biological relevance of vessels produced using this scheme compared to the endothelial-cell-attachment scheme. Moreover, the shape and dimensions of these capillaries cannot be precisely controlled, unlike the EC-attachment scheme on a micropatterned hydrogel. Refining the scheme for engineering defined capillary structure is required for future studies that use a media perfusion system to apply a physiological level of flow to the capillaries.

2.4 Motivation and objectives

Using the angiogenic/vasculogenic properties of ECs, two experimental platforms that form perfusable 3D microvessels based on spatially controlled co-culture of endothelial cells with stromal fibroblasts were reported [41, 42]. As they were generated by the natural angiogenic/vasculogenic process, the models share closer biological relevance to the real blood vessel compared to many previous models that utilizes EC attachment to the pre-established hydrogels or trans-membranes. However, these models also share several limitations for establishing various vascular biology models. For vascular permeability assay, perivascular region should be susceptible to the fluorescent molecule diffusion. The platform of Yeon et al., however, has perivascular region with PDMS channels filling, which makes the time-dependent monitoring of fluorescent molecules diffusion impossible. The platform of Kim et al. showed much pertinent perivascular region for the vascular permeability assay. However, as the generation of the vascular network is random, determining ROI for the vascular permeability assay becomes laborious, and data contamination by the fluorescent molecules diffused from the adjacent microvessels make the assay unreliable and unreproducible.

Furthermore, in order to establish cancer angiogenesis/metastasis models, perivascular region should be accessible for the introduction of the other cells

after the microvessel formation. However, the two platforms could not be used for establishing the cancer angiogenesis/metastasis models as their perivascular region is inaccessible after the microvessels were made in the chip. Therefore, geometrically optimized microvessels are needed for further establishment of the various vascular biology models.

II. DEVELOPMENT OF A MICROFLUIDIC PLATFORM FOR HIGH-THROUGHPUT VASCULAR PERMEABILITY ASSAY

1. Advantage of this platform

This microfluidic-based platform presents a simple and rapid method for assessing drug effects on blood vessel permeability. This microfluidic chip implemented a design that guides formation of a perfusable array of vessels in separate chambers, facilitating high-throughput measurement of permeability. Guided angiogenic sprouts form fully lumenized microvessel tubes that can be connected to external fluidics for reliable measurement of permeability under various conditions [44].

2. Materials and methods

2.1 Cell culture

Lung fibroblasts (LFs, Lonza, Switzerland) were cultured in Fibroblast Growth Medium (FGM-2, Lonza, Switzerland) and passages 5 to 7 were used for the experiments. Human umbilical vein endothelial cells (HUVECs, Lonza, Switzerland) were cultured in Endothelial Growth Medium (EGM-2, Lonza, Switzerland) and cells in passages 5 to 6 were used. Human glioblastoma cells, U87MG (ATCC, Virginia), were cultured in DMEM (Hyclone) supplementedwith 10% FBS, penicillin (100 U/ml) and streptomycin (100

U/ml). All cells were maintained in a humidified incubator at 37 °C and 5% CO2.

2.2 Microfluidic chip fabrication

Silicon wafers were coated with 50 μm thick SU-8 (MicroChem, Newton MA) and patterned to generate a master mold. PDMS chips were fabricated by replica molding against the master mold. Holes were punched out with cylindrical biopsy punches and sharpened blunt hypodermic needle for media reservoirs and cell injection ports, respectively. The PDMS and cover glass slides were then plasma treated and irreversibly bonded. The bonded chips were kept in 80 °C dry oven for 48 h to make the surfaces of PDMS channels hydrophobic. The chips were sterilized with UV for 2 min before use. Computational simulation of gel filling process was performed with COMSOL Multiphysics (COMSOL, Burlington, MA).

2.3 Hydrogel and cell loading

Hydrogels and cell containing hydrogels were selectively injected into the microchannels following a method previously described [45]. Briefly, LFs and U87MG were harvested from tissue culture dishes and resuspended in bovine fibrinogen solution (2.5 mg/ml fibrinogen with 0.15 U/ml aprotinin) mixed

with thrombin (0.5 U/ml) and injected into the stromal cell channel. Concentration of LFs and U87MG were 10 million/ml. Fibrinogen solution (2.5 mg/ml fibrinogen with 0.15 U/ml aprotinin) mixed with thrombin (0.5 U/ml) without the cells was injected into the vessel channel. After waiting for 2 min to allow for fibrin gelation, media reservoirs were filled with EGM-2 media and gently aspirated to media channels 1 and 2. Next day, HUVECs resuspended in EGM-2 media (10 million/ml cell concentration) were gently loaded into media channel 1. The chips were tilted for 40 min to allow HUVECs to settle and attach to the fibrin gel sidewall that fills the vessel channel. The chips were incubated for 6–7 days until fully lumenized microvessels formed.

2.4 Microscopy

An inverted microscope (Olympus IX81) equipped with a CoolLED fluorescent light source was used for fluorescence microscopy. Confocal microscope (Olympus FV1000) was used for obtaining three-dimensional z-stack image of immunostained samples. IMARIS (Bitplane, Switzerland) was used for three dimensional image constructions. The microscope and CCD camera were controlled with MetaMorph (Molecular Devices, USA) for time-lapse and multi-stage imaging.

2.5 Immunostaining

Samples were washed twice with phosphate-buffered saline (PBS, Hyclone, USA), and fixed with 4% (w/v) paraformaldehyde in PBS for 15 min. Cells were permeabilized with 0.15% Triton X-100 (Sigma-Aldrich, Korea) solution in PBS for 15 min. After treating with 3% bovine serum albumin (BSA, Sigma-Aldrich, Korea) and Hoechst 33342 (1:1000) in PBS for 1 hour, the cells were stained with Alexa Fluor® 594 conjugated mouse monoclonal antibody against ZO-1 protein (Molecular Probes). Alexa Fluor® 488 conjugated mouse monoclonal antibody against Claudin-5 (Invitrogen) and VE-cadherin (eBioscience) protein to visualize tight junction.

2.6 Permeability factor treatments

Recombinant human TNF-α was purchased from PeproTech. All the factors were diluted into EGM-2 medium with adjusted concentration. TNF-α treatment experiments were performed at day 6. The vessels were exposed to 20 ng/ml or 40 ng/ml of TNF-α for 24 hours before permeability measurement.

Histamine was purchased from Sigma-Aldrich. Histamine treatment experiments were performed at day 7. The microvessels were exposed to 100 μM of histamine for 40 minutes before permeability measurement.

VEGF was purchased from R&D systems. VEGF treatment experiments were performed at day 6. The microvessels were exposed to 80 ng/ml of VEGF for 24 hr before permeability measurement.

2.7 Anti-VEGF neutralization

For neutralization of VEGF activity, we used bevacizumab, (Avastin, Genentech), an antibody that specifically neutralizes human VEGF. Bevacizumab was diluted to 2.5 mg/ml with EGM-2 and added to the media reservoir in the microfluidic chip. Same volume of PBS was added without bevacizumab for control experiments. Treatments with bevacizumab were maintained over 24 hour periods starting at day 6.

2.8 Permeability coefficient measurement

Fluorescence images of FITC-dextran diffusion across the vessels were analyzed to calculate the permeability coefficient. After removing all the media in the reservoirs using 1 mL pipette, 20 μl of FITC-dextran solution was introduced into one of the media reservoirs. As the microvessel has lumenized enough to allow solution into their lumen, the FITC-dextran molecules were introduced into the microvessel lumen by hydrostatic pressure. A picture with 20x objective was taken that show entire vessel in a single shot every 15 sec

interval. All the microvessels on one chip were imaged using multi-stage time-lapse mode in Metamorph.

In the previous study [46], the permeability coefficient equation is described as:

$$P = (1 - H_t)\frac{V}{S} \times \frac{1}{I_0} \times \frac{dI}{dt}$$

Where H_t is average hemocrit in the microvesel, V and S are the total volume and surface area of the microvessel, dI/dt is the total fluorescence intensity change per unit time, and I_0 is the intravascular fluorescence intensity at the time of the fluorescence solution injection.

In our system, the microvessel region and perivascular region is separated with a layer of vessel wall. Therefore, we modeled this system as two chambers separated by a membrane (vessel wall). The assumption was based on Fig. 2.7 which shows the microvessel filling almost entire height of the channel. With this assumption,

$V = A \times h$ (A = area of the microvessel in the x-y plane, h = height of the channel)

$S = l_w \times h$ (l_w = length of the vessel wall that separates between perivascular and microvessel region)

$H_t = 0$ as there is no hemoglobin in the microvessel.

Substituting the equation with these factors, the equation was modified as:

$$\mathrm{P} = \frac{Ah}{l_w h} \times \frac{1}{I_0} \times \frac{dI}{dt} = \frac{1}{l_w} \times \frac{1}{I_0/A} \times \frac{dI}{dt} = \frac{1}{l_w} \times \frac{1}{I_i} \times \frac{dI}{dt}$$

where I_i is mean fluorescence intensity in the microvessel region.

For measuring dI/dt, area close to the vessel was chosen and the change in total intensity inside the area was measured from fluorescence microscopy images as a function of time. During the acquisition of fluorescence intensity, I_i was constant as there was slow constant flow of FITC-dextran solution in the vessel lumen by the hydrostatic pressure. However, as the total time that the flow affects the microvessel is less than three minutes, we assumed it is not sufficient to affect the barrier function of the microvessel and neglected that effect. The captured images were analyzed and quantified with Image J. To ensure that all the fluorescent molecules that have crossed the vessel barrier are taken into account (remaining inside the chosen area at the perivascular region), total length of acquisition time was kept to a minimum (acquiring every 15 sec for 90-120 second period).

To test the effect of multiple time-lapse image acquisition on photobleaching, we continuously exposed FITC-dextran filled vessel for 10 sec. The fluorescence image taken after extended exposure indicated

negligible decrease in fluorescence intensity (less than 1%). Considering the total exposure time was less than 2 sec (250 msec/acquisition x 8 acquisitions), photobleaching of dye due to image acquisition is negligible.

3. Results

3.1 Schematic of the microfluidic chip

The chip was designed to engineer an array of single microvessels that facilitate high-throughput microvessel permeability measurements. Fig. 2.1 shows the schematic of the chip which consist of 4 distinct channels. The vessel chambers are located in the middle and each chip contains 7 identical separate “boxes” where a single microvessel is situated and independent permeability measurements are made. The vessel chamber is flanked by two symmetrical medial channels that are connected to 4 large media reservoirs in the periphery. Detailed schematic of the layout in Fig. 2.1 shows stromal cell channel (SCC) on the far right side that is separated from the media channel by a row of posts. The device was designed to allow selective filling of each four channels with different gels, cells, or media [42, 45]. The central channel is first filled with 3D fibrin gel (width=550 μm) and later occupied by microvessel that sprout from the media channel 1 (MC1) toward (MC2). Width of the media channels are 850 μm. The sprouting direction is controlled

by filling stromal cell channel (SCC) with LFs or U87MG on the right to produce mixture of growth factors that form a gradient across the vessel channel. Since the EC sprouts grow toward the source of growth factors (secreted by cells in stromal channel), the media channel width was optimized to be long enough to minimize LF migration into the vessel chamber while short enough for paracrine signaling.

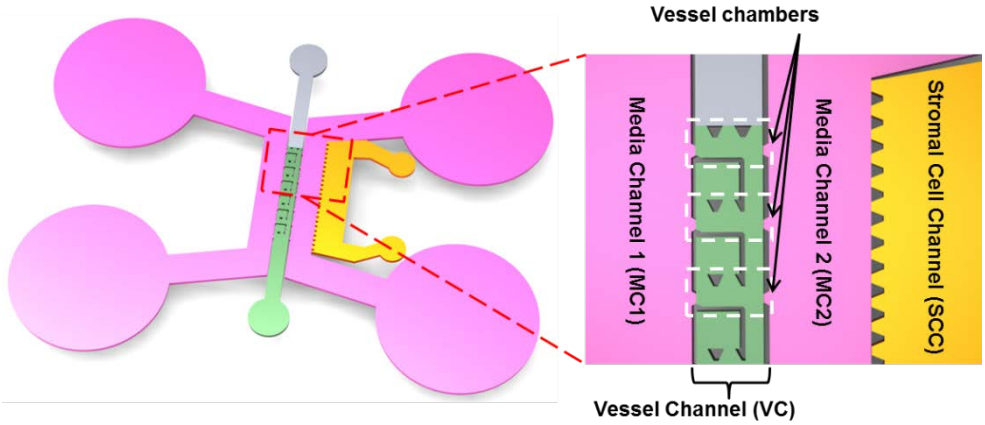

Figure 2.1 Schematic of the microfluidic chip for microvessel engineering. The vessel chambers were designed to guide sprouting ECs to form a continuous single sprout that traverses the width of the vessel channel (550 μm), connecting media channel 1 to media channel 2. Height of the channels was 50 μm and post-to-post distance was 70 μm. When ECs are placed on left sidewall of vessel channel (which is filled with fibrin), they sprout toward the stromal cell channel direction.

Each vessel chamber within the VC contains box-like structures that were designed to guide the HUVEC sprouts such that a straight single, non-branched vessel is formed. Since each “box” structure is separated from each other, isolated vessel chambers enable independent multiple permeability measurements on a single chip. Up to seven separate isolated vessel chambers were designed to form multiple microvessels in parallel. The channel heights were maintained at 50 μm and the micropost (outside) gap to gap distance at 70 μm. These changes allowed successful filling of seven chambers in a single step by steering gels into each chamber serially.

Fig. 2.2 shows the computational simulation of the gel filling process. When a liquid is introduced from the bottom, it fills each vessel channel sequentially one at a time before filling the next chamber. Hydrophobic surface of the inner channel and close distance between posts prevent gels from bursting into the side media channels. This is an important design parameter as incomplete filling of chambers result in defective devices where no 3D matrix is present for EC sprouts to grow through. The vessel chamber walls are composed of “open box structures” with a post on the bottom. If the boxes are composed of solid wall without any opening, the microvessel will fill the channel without leaving any perivascular region with fibrin. As shown in our previous work [41], such design does not allow permeability measurement as the PDMS wall confines the perivascular region and there is no region for FITC-dextran to diffuse out. Therefore, by designing hollowed

wall with a post, microvessels can be confined by the PDMS wall and post while retaining the perivascular region with fibrin gel.

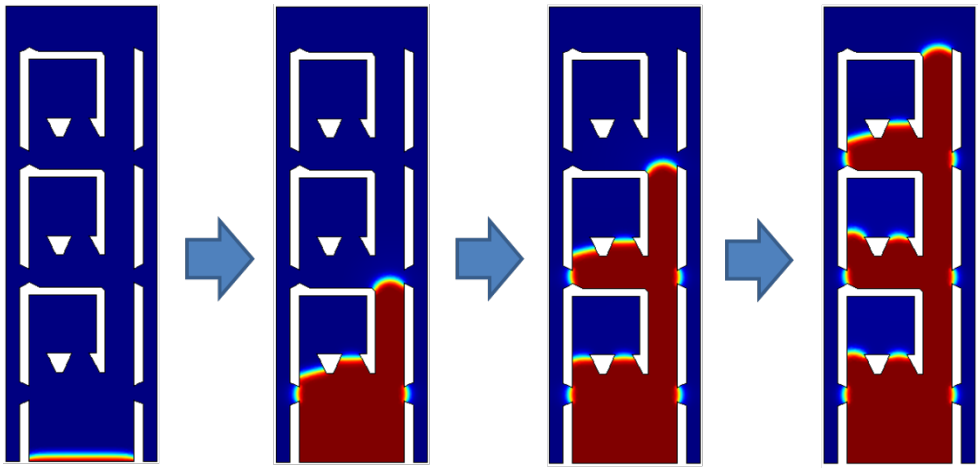

Figure 2.2 Computational simulation of the gel filling inside the vessel channel. Fibrin gel fills each vessel chamber one by one as the fluid advances.

Fig. 2.3 shows a phase contrast micrograph of the chip after filling the vessel channel with fibrin gel and filling SCC with cells. ECs placed on the left sidewall of the vessel channel can also be observed. The micrograph shows that the vessel chambers are selectively filled with fibrin gel in the same pattern as modeled with computational simulation while the open “box structures” are trapped with air. It takes approximately 1.5 hours to prepare 36 microfluidic chips filled with fibrin and LFs in SCC. Microvessel formation following angiogenic sprouting occurs over next 6-7 days after which the permeability measurements are made.

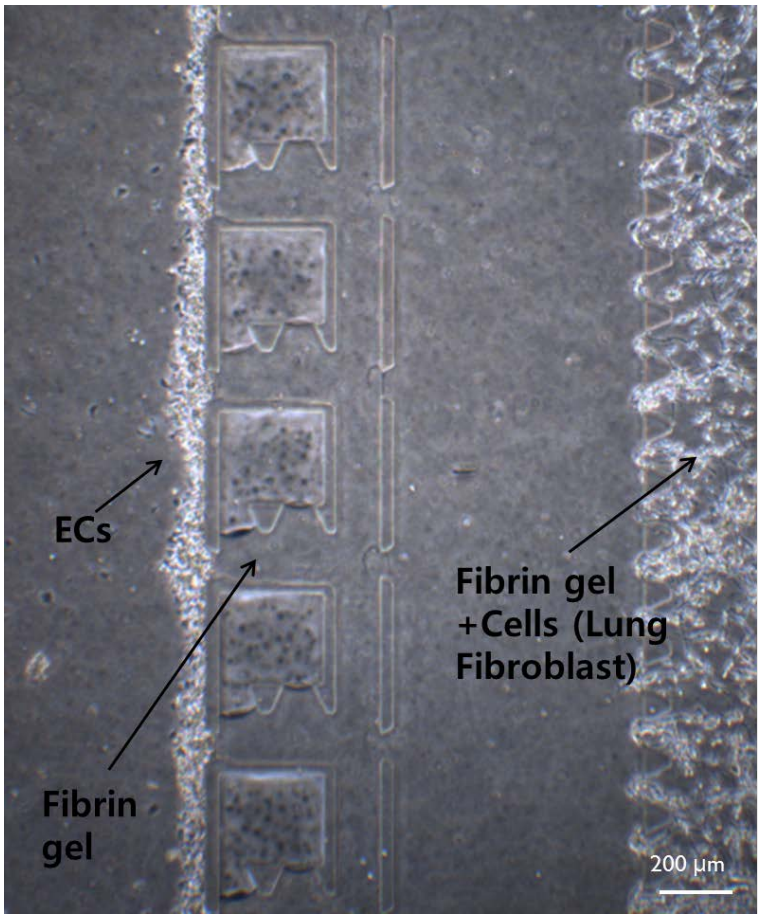

Figure 2.3 Micrograph of the gel and cell loading into the microfluidic chip. Experimental result of fibrin filling closely follows the simulation result. Fibrin gels and stromal cells can be patterned in respective areas and ECs are attached to the sidewall of the vessel channel. By incubating this fully loaded chip, we can engineer the microvessel array.

3.2 HUVEC sprouting across vessel channel induced by LF

HUVECs have been widely used in a number of previous vessel permeability studies [16, 47, 48]. In this study, we took advantage of HUVECs to generate reproducible 3D microvessels for permeability measurements. Design of the chip was focused on engineering multiple perfusable 3D microvessels in a microfluidic environment that allow direct manipulation and exchange of fluids for permeability measurements. Stromal cells such as LF and U87MG cells plated in SCC secrete various angiogenic factors and cause ECs plated on the sidewall to sprout vessels across the vessel chamber. We used LFs as stromal cells to model angiogenesis in normal conditions (Fig. 2.4) while U87MG cells for tumor associated vessel angiogenesis.

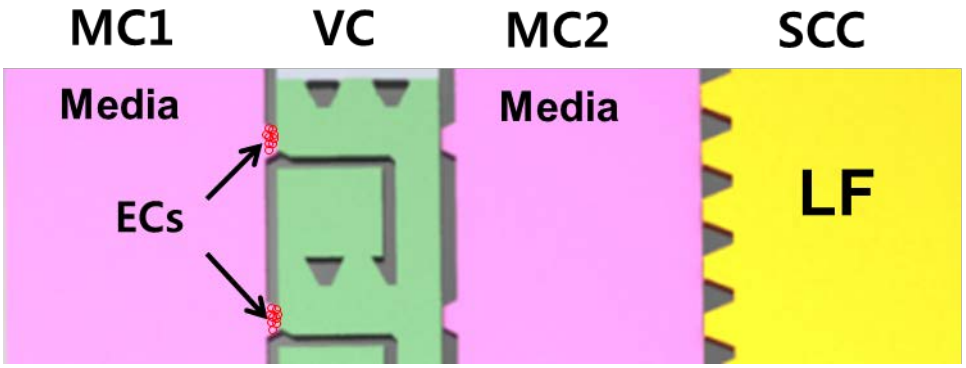

Figure 2.4 The experimental setup for inducing microvessel with LF. At the stromal channel, LF was introduced as a stromal cell for inducing the microvessel growth.

Fig. 2.5 shows a series of micrographs at days 2, 4 and 6 as the vessels sprout and grow across the vessel chamber. Two days after the HUVECs are attached on the sidewall, several small sprouts are seen inside the vessel chamber area. In some cases, the cells have invaded and migrated across the entire 550 μm width and reached the opposite side. At this point, the sprouts have not formed complete lumens and the vessels have not merged to form a continuous EC tube.

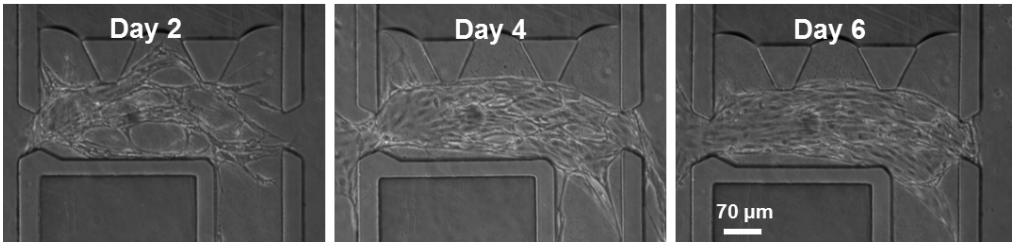

Figure 2.5 Day by day image of the microvessel growth in the chip. HUVEC sprouts grow from left sidewall of vessel channel toward LF channel on the right (not shown). On day 2, many small sprouts are seen in the vessel channel. These sprouts have not formed lumen and are not connected. On day 4, some sprouts reach the opposite end of the vessel channel and show signs of lumen formation. Some small branches are observed. On day 6, the lumen formation is completed and it spans the whole length of the vessel chamber with openings to media channels on both ends. At this point, small sprouts are fused into a single microvessel.

By day 4, most HUVEC sprouts reached the opposite side of the vessel chamber. In most cases, a single tube which is formed in VC area with occasional occurrence of merged vessels is observed. Few branches and sprouts that will regress over next few days are still visible from the main vessel. From our experience, only a fraction of the vessels are perfusable at day 4.

Majority of the vessels have grown across the vessel chamber and are fully lumenized by day 6. Because both ends of the vessels are open and connected to media channels, access into the lumen is possible and different solutions can be perfused at this state.

Diameter of the microvessels formed by angiogenesis increased slightly forming a tubular structure with a lumen that has ~100-150 μm width (height confined by the channel height 50 μm). In this report, the microvessels consist of HUVECs without pericytes and other cell types, and the inner space of the microvessels are empty and patent. Shapes of the microvessels remain constant and do not show any signs of regression or collapse for up to 14 days or longer.

To confirm the effect of stromal cells on vessel formation, we performed HUVEC sprouting experiments without LF in SCC. As expected, HUVECs do not form viable sprouts after 6 days (Fig. 2.6a). No perfusable vessels were found in total of 18 chips tested without LFs. When additional VEGF

(80 ng/ml) was added to media on MC2 to partially replace VEGF secreted by LFs, few sprouts were observed to cross the vessel chamber at day 6 (Fig. 2.6b). By examining total of 18 chips with the VEGF condition, these vessels turned out to be defective in forming patent lumen and could not be perfused and thus not viable for permeability measurements. Although the results were slightly promising with soluble VEGF addition when compared to control experiments without LFs, no viable vessels were obtained. From these experiments, we confirmed the essential role of stromal cells for engineering robust microvessels suitable for the vascular permeability assay.

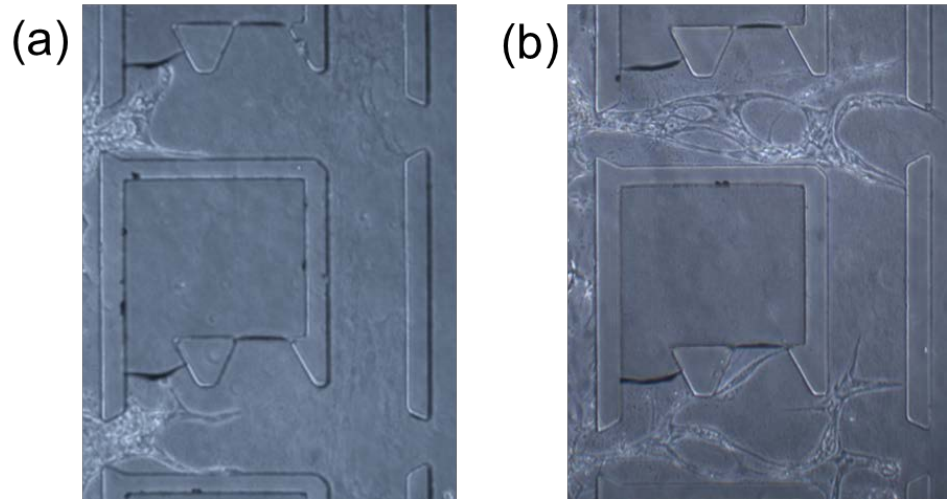

Figure 2.6 HUVEC sprout inducing without LFs. (a) HUVECs without LF at day 6. The HUVECs could only made small and short sprouts and were not able to traverse across the vessel channel. (b) HUVECs with VEGF gradient (80 ng/ml at the media channel 2) at day 6. Although the sprouts could reach the other end of the vessel channel, they did not have patent lumen and could not be used for the permeability assay.

3.3 Formation of tight junctions observed with immunostained junctional proteins

After perfusable microvessels are formed, they were fixed at day 6 on the microfluidic device and stained with nucleus marker Hoechst 33342 (blue) and tight junction marker ZO-1 protein (red). Fig. 2.7 shows confocal microscope image of ZO-1 protein expression and their three-dimensional distribution in the microvessel. Cross-section images of the microvessel (Z-sectioned at three different positions along the vessel indicated by 1,2, and 3) showed tubular structure with open lumen. Shape of the vessels was rectangular because they were confined by the PDMS. This image clearly demonstrates that the microvessels are composed of open tube structures that connect opposite ends of the vessel chamber, forming a perfusable patent vessel.

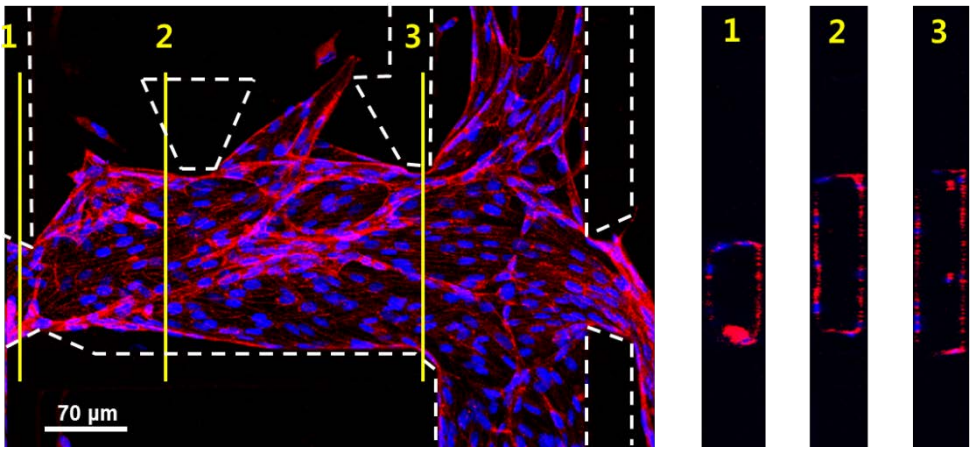

Figure 2.7 Immunostaining for ZO-1 (tight junction protein) with three dimensional stacking. The image shows clear expression of tight junction. Cross sectional views at 3 different positions along the vessel chamber confirm complete formation of one continuous lumen. White dotted line shows the PDMS structure.

High-resolution micrographs of cell-cell junctions stained for 3 different junctional markers are shown in Fig. 2.8 (upper left: ZO-1, upper right: Claudin-5, lower: VE-cadherin). These immunostained images show robust and strong expression of junctional proteins. Furthermore, the elongated morphology of the endothelial cells is similar to capillary-like structures found *in vivo* [49], which is markedly different from the random morphology shown in 2D EC monolayers [33, 50]. These microvessels engineered on the microfluidic chip by natural angiogenic sprouting can be a suitable model for vascular permeability assays as they have similar junctional characteristics to that found *in vivo*.

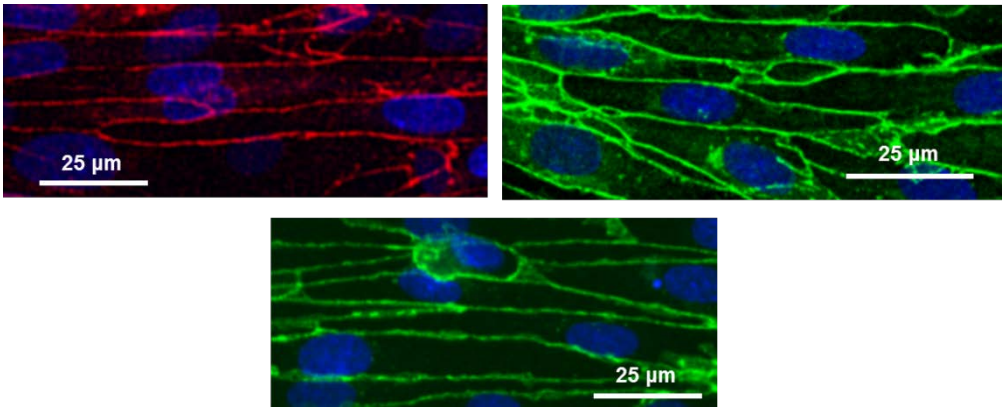

Figure 2.8 Fluorescence imaging of junctional proteins. High magnification micrograph of the ZO-1 (upper left), Claudin-5 (upper right), and VE-cadherin (lower) expression shows that the tight junction is clearly expressed around cell–cell junctions.

3.4 Vascular permeability measurement

Microvessel permeability measurements were performed at day 6. Due to redundancy built into the chip design (7 separate vessel chambers), up to seven vessels can be formed simultaneously. In practice, 3.25 ± 0.63 vessels (mean ± standard error, 12 chips were tested) were lumenized and opened to the both side of the media channels and could be used for the permeability assay.

Before starting the measurement, each chip's reservoirs were emptied and filled with solution containing fluorescent dye. Series of time-lapse images were acquired with 20x objective at each vessel chamber. Fig. 2.9 shows a series of fluorescence micrographs at 10, 115, and 235 seconds after introducing FITC-dextran (20 kD). With time, perivascular region around the vessels showed slight increase in fluorescence intensity due to FITC-dextran that has passed through the microvessel barrier. Weak fluorescence signal is due to small amount of dye that is passing through the microvessel barrier. If some large defects are present at the barrier, massive leakage of the dye was observed around the perivascular region immediately following dye injection. In contrast to previous study by Tien et al. focal leaks were not observed in our model [33].

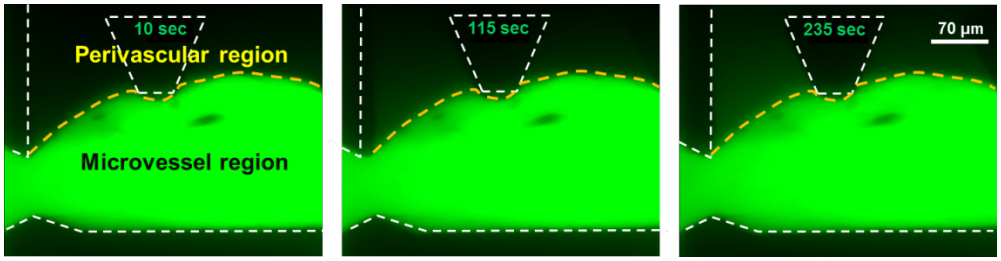

Figure 2.9 Vascular permeability measurement with fluorescence micrographs of vessel filled with FITC-dextran. Time series fluorescence micrographs were taken and analyzed for intensity changes in the perivascular region to measure permeability. Yellow dotted lines represent boundary between microvessel and perivascular fibrin gel. White dotted lines show the PDMS structure.

A line scan intensity plot was used to confirm diffusion of fluorescent molecule across the vessel barrier and into the perivascular region. Fig. 2.10a shows a graph of fluorescence intensity change as a function of distance away from the vessel wall. The intensity signals at time 115 sec and 235 sec were background corrected with values obtained at 10 sec. Similar to results seen in the fluorescent micrographs, the intensity curve shows increasing intensity with increasing time, indicating increasing concentration of dye molecules.

FITC-dextrans (4 kD, 20 kD and 70 kD) were used to measure endothelial barrier permeability as a function of molecular weight (Fig. 2.10b). Permeability coefficient values decreased with higher molecular weight of FITC-dextran, in agreement with previously published studies [8, 11, 15, 16].

Although the permeability coefficient calculated in this study is slightly higher than the value reported from an in vivo model ($0.15 \times 10^{-6}\ cm/s$ for 70 kD FITC-dextran) [11], it is close to that obtained from isolated mammalian venules (approximately $2 \times 10^{-6}\ cm/s$ for 70 kD FITC-dextran) [51]. In addition, permeability coefficient obtained in this work is two to three times lower than the coefficients measured in many previous *in vitro* blood vessel models (approximately $4 \times 10^{-6}\ cm/s$ for 70 kD FITC-dextran) [13, 16, 36].

Tumor necrosis factor-α (TNF-α) is a pro-inflammatory cytokine that increases vascular leakage and has been shown to increase permeability of

endothelial monolayer [52-54]. To characterize barrier property change in response to exogenous factors, we exposed the microvessels to TNF-α (20 ng/ml and 40 ng/ml) for 24 hours. After treatment, permeability of the microvessel was measured using 70 kD FITC-dextran. Permeability coefficient of the microvessels was about 1.6~2 times increased with increasing concentration of TNF-α (Fig. 2.10c). TNF-α effect on permeability is in agreement with the trend that has been observed previously [12, 52, 55].

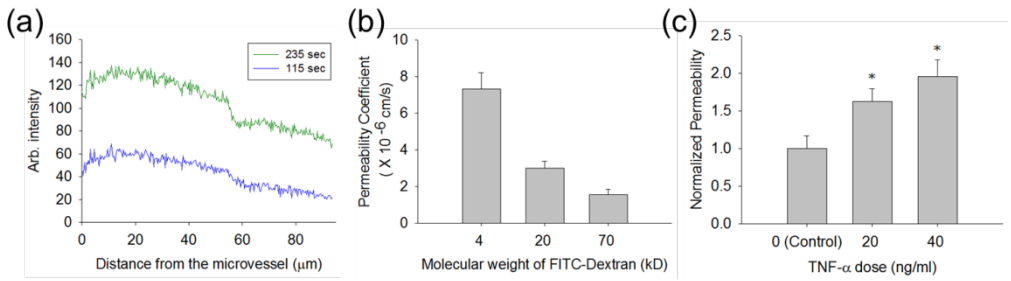

Figure 2.10 Quantification of the permeability responses. (a) Line scan of fluorescence intensity away from the vessel in the perivascular region. The values are normalized with fluorescence intensity at initial time point. Increasing fluorescence intensity with time indicate increasing amount of dye that have crossed the vessel barrier. (b) Permeability coefficient for different molecular weights of FITC-dextran (n = 4 for each condition). Permeability coefficient decreased with increasing molecular weight, as expected. (c) When exposed to inflammatory cytokine, TNF-α, permeability increased in dose-dependent manner (n = 5 for each condition, *p b 0.05 compared to control). Error bars represent SEM.

The hydraulic pressure difference between microvessel region and perivascular region can induce additional FITC-dextran molecule dissemination, tainting true diffusive vascular permeability data. Decoupling the effect of solvent drag for obtaining true diffusive permeability coefficient has been performed in *in vivo* studies [11, 56]. In contrast to these studies, the flux of the solution from the microvessel region towards the perivascular region will not significantly affect the permeability coefficient as the perivascular regions are confined with PDMS walls. However, if the flow rate (or shear stress) of the FITC-dextran solution inside the microvessel is extremely high compared to physiological level, we cannot guarantee that the pressure difference between the endothelium is negligible. Therefore, to confirm the hydrostatic pressure-induced flow rate in the microvessel is not unusually higher than physiological level, we calculated the hydrostatic flow rate and the shear stress by the following equations:

$$\Delta p = \frac{8\mu LQ}{\pi R^4} \quad \text{(flow-pressure relation in a tube)}$$

$$\tau = \frac{4\mu Q}{\pi R^3} \quad \text{(Shear stress induced by flow in a tube)}$$

By assuming that the microvessels have a perfect tube shape with a radius of 50~100 μm, and the chip has three vessels on average, initial shear stress from the hydrostatic pressure difference of 20 μl FITC-dextran solution is

$9\sim19$ dyne/cm^2. This is not significantly high compared to physiological shear stress level ($40\sim60$ dyne/cm^2 in the arterioles and capillaries or $10\sim20$ dyne/cm^2 in large arteries and venules, [57]). Therefore, effect of the solvent drag is negligible in this experimental condition.

3.5 Microvessel induced by U87MG and their permeability response to bevacizumab treatment

To investigate the vascular permeability of tumor-associated vessels, U87MG, a glioblastoma cell line with high angiogenic potential [10, 58], was used as stromal cells in place of LFs (Fig. 2.11). Fig. 2.12 shows HUVEC sprouts induced by U87MG reached the other end of the vessel channel and fully lumenized at day 6. Vascular permeability of the tumor microvessels was measured in same manner as discussed above for LF-induced vessels.

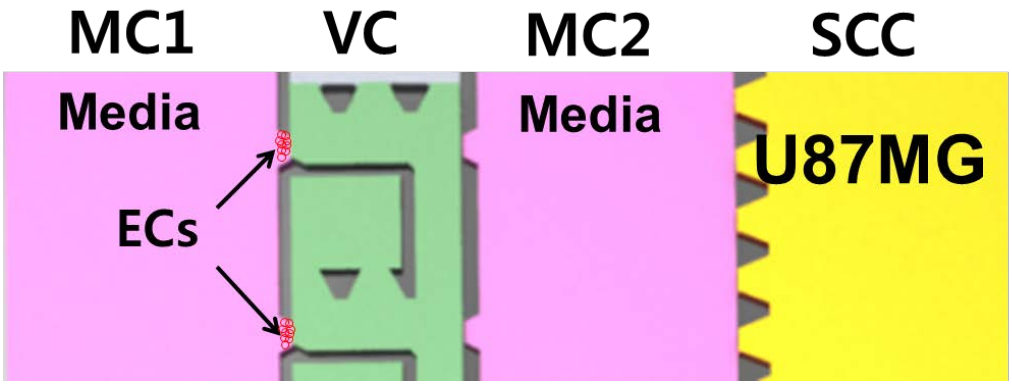

Figure 2.11 The experimental setup for inducing microvessel with U87MG. At the stromal channel, we introduced U87MG as a stromal cell for inducing the microvessel growth.

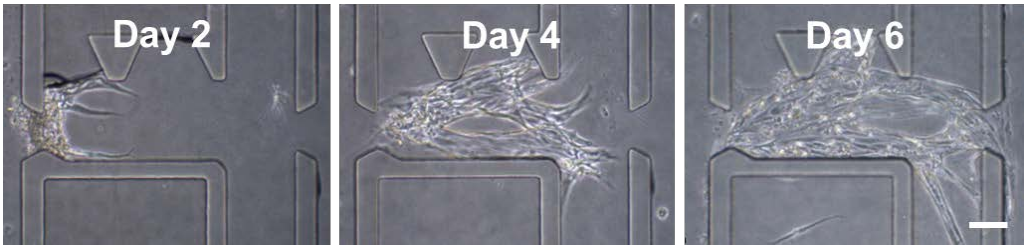

Figure 2.12 HUVEC sprout growth induced by U87MG. On day 2, a number of EC sprouts are growing toward the other end of the vessel channel. In the beginning, the growth of HUVEC sprouts induced by U87MG is slower compared to LF-induced sprouts. However, on day 6, the sprouts also reach the other end of the vessel channel and are fully lumenized. At this time point, similar to the sprouts induced by LF, the EC sprouts are fused and become one microvessel, filling each vessel chamber.

Fig. 2.13 shows relative vascular permeability of microvessels induced by LF and U87MG and those treated with anti-VEGF antibody, bevacizumab. As expected, U87MG induced vessels show significantly higher permeability compared to LF induced vessels (Fig. 2.14). Structure of the tight junction protein (ZO-1) of the U87MG-induced microvessels showed abberant morphology with disrupted continuity, confirming the disruption of cell-to-cell junctional expression (Fig. 2.15). The treatment of bevacizumab to the U87MG-induced microvessels significantly lowered the vascular permeability, while the effect of treatment of bevacizumab to LF-induced vessels was not statistically significant. This clearly shows the effect of excessive VEGF secreted from U87MG to the vascular permeability.

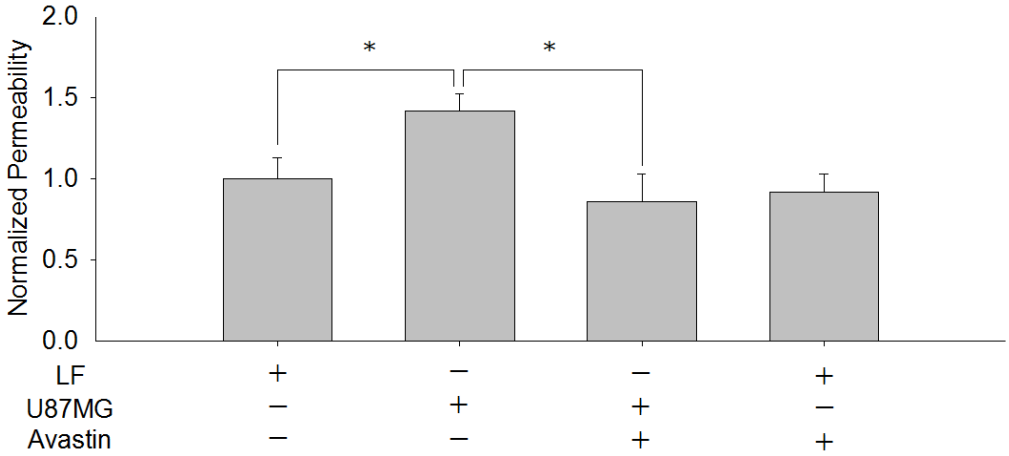

Figure 2.13 Permeability of the microvessels induced by U87MG and the bevacizumab treatment. Permeability of the microvessels induced by U87MG was significantly higher than that of LF-induced microvessels. Bevacizumab treatment dramatically decreased the permeability of microvessels induced by U87MG. This result closely mimics the normalization process of tumor blood vessels by anti-VEGF therapy in vivo (n = 6–9 for each condition, *p b 0.05). Error bars represent SEM.

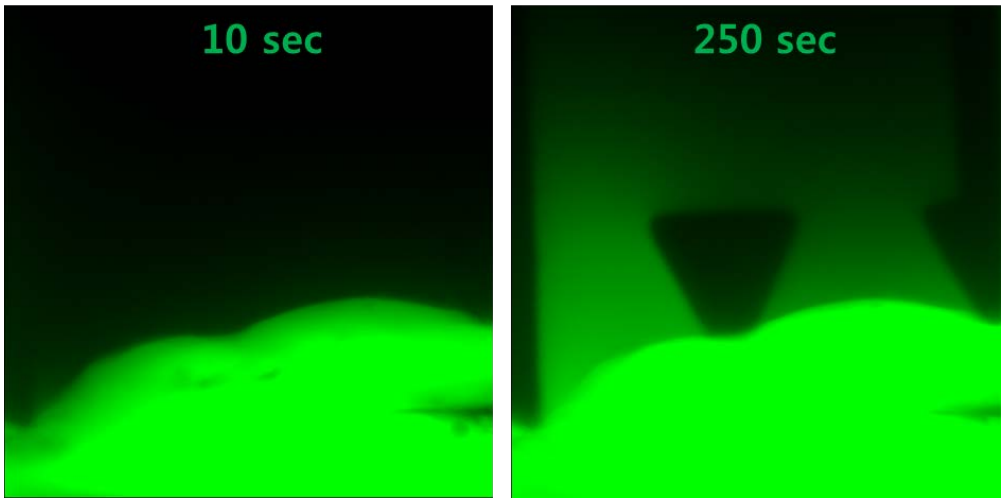

Figure 2.14 Permeability imaging of the microvessel induced by U87MG. The micrograph shows faster diffusion of 20kD FITC-dextran to the perivascular region of U87MG-induced microvessel.

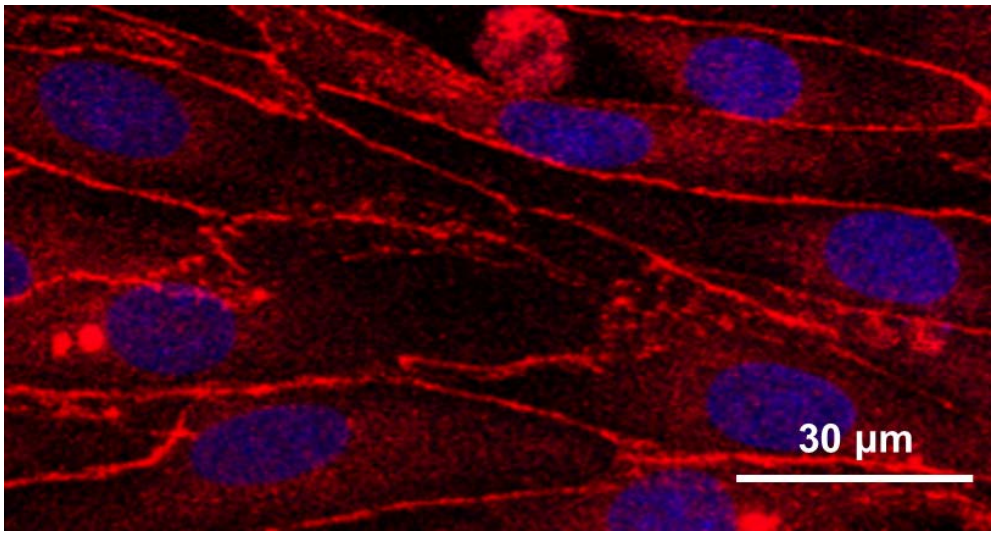

Figure 2.15 Junctional imaging of the microvessel induced by U87MG. ZO-1 expression of the U87MG-induced microvessel has abberent and discontinuous morphology, showing the disruption of cell-to-cell junctions.

The fact that bevacizumab treatment had drastically lowered and normalized the permeability of U87MG induced vessels is remarkable. This data indicate that the hypermeability of the tumor-associated vessels are mainly due to VEGF (secreted by U87MG) and it can be regulated by anti-VEGF treatment. Since the cancer cells secrete higher amount of VEGF compared to other cells, capillaries near the tumors show higher permeability than capillaries in normal tissues, and can be normalized by treatment with anti-VEGF [49, 50, 58].

4. Discussion

A simple reproducible permeability assay based on a microfluidic device was developed. On a single chip, array of multiple perfusable microvessels with 3D open lumen is engineered that exhibit barrier functions and reactivity to the factors such as TNF-α, histamine or VEGF. For a typical experiment, 36 chips were fabricated and used. It takes about 1.5 hours to set up a set of experiment including preparation of the cells and loading them into the chips. This experimental process involves simple pipetting of cell-fibrin mixture into the channels and waiting for vessels to form after 6-7 days. On average, three perfusable vessels without major leakage are formed on each chip. Thus we consistently obtain around 100 vessels suitable for testing permeability with different factors. Experimental simplicity and potential for compatibility with high-throughput experiments are two main advantages of this device compared to conventional assays.

Compared to previously reported vascular network model [42], the design used in this work has several advantages stemming from capacity to generate an array of separate single straight vessels instead of complex random overlapping vessel network. First, single straight vessels combined with structural guides implemented in this work allow reproducible assignment of ROI (region of interest) possible for permeability measurement. Second, separate vessel chamber "boxes" isolate vessels from each other on the same chip and enable precise permeability measurement without contamination from adjacent vessels that has macroscopic leakage. In the old design a single complex network was formed and leakage at any one position resulted in an experiment unsuitable for permeability measurement, significantly lowering the yield. Third, up to seven chambers are integrated in one chip with an average of three vessels for measurement, greatly increasing throughput. Fourth, lower channel height (50 μm compared to 100 μm in previous designs) allows better sealing by the EC monolayer at both ends of the vessels with the device and minimize leakage. Higher channels increase the chance of incomplete EC monolayer formation on the sidewall and cause major leaks into perivascular region from media channel 1.

The vessels expressed pertinent level of junction proteins, ZO-1, Claudin-5 and VE-cadherin around the cell-cell junctions, and the vessels exhibited tight barrier function, with an estimated permeability for 20kD FITC-dextran of 3.0×10^{-6} cm/s, which is in a range of intact or explanted mammalian

venules in vivo [51, 59, 60]. The vessels showed decreasing permeability with higher molecular weight macromolecules.

The diffusion rate of the FITC-dextran in the media and fibrin gel is different. In this work, however, barrier function of the microvessels is quantified by measuring the intensity of the FITC-dextran at the perivascular region, not by the diffusion length of the FITC-dextran in the perivascular region. That is, the diffusion rate of the FITC-dextran in the fibrin gel does not affect the quantification of the vascular permeability, as the value is determined by the intensity of the FITC-dextran in the perivascular region, no matter how the molecules are diffused in the perivascular region. Therefore, the diffusion rate of the FITC-dextran in the fibrin gel is not considered for the quantification of the vascular permeability.

When exposed to an inflammatory mediator such as TNF-α or histamine, permeability coefficients of the microvessels increased significantly, which agrees with previously published studies [12, 52, 55, 61]. Hyperpermeability is a factor responsible for cancer progression, as the leaking plasma proteins in perivascular region can lay down provisional matrix for endothelial cell migration toward the cancer colony [62]. Cancer blood vessel normalization using anti-VEGF therapy has been one of the major approaches for fighting cancer [10, 63-65]. In this study, we have successfully modeled hyperpermeability of cancer blood vessel by using U87MG cancer cells.

Application of bevacizumab to tumor-associated vessels dramatically improved barrier function with permeability value similar to normal vessels (Fig. 2.13). Normalization of U87MG-induced microvessel permeability with bevacizumab treatment suggests that a possible reason for ZO-1 disruption in U87MG-induced microvessels (Fig. 2.15) may have been caused by excessive secretion of VEGF from U87MG. This is also supported by a previous study that shows ZO-1 disruption by the excessive treatment of VEGF to an EC monolayer [66]. As these preliminary studies with bevacizumab, TNF-α and histamine agree with previous in vivo studies [10, 12, 52, 55, 61], we envisage that these *in vitro* microvessels can reliably predict *in vivo* response to various stimuli and potentially be useful in drug screening applications.

Several subordinate conditions for determining dimensions of PDMS structures in one of the vessel chamber in the vessel channel is shown in Fig. 2.16. Dimensions that have to be considered are represented in an alphabet. Dimension A should be at least smaller than 100 μm in order to reliably trap the fibrin gel into the vessel channel. The smaller the dimension A, the higher success rate for trapping the gel. However, if the dimension A is too small, paracrine interaction between EC and LF becomes attenuated. Dimension B should be larger than A, as the fibrin gel should be filled through the dimension B while not crossing the dimension A. In the same manner, dimension C should be larger than dimension B as the fibrin gel should cross the dimension C before traversing dimension B. Dimension D should be

smaller than 100 μm at least, in order to secure the perivascular region without fibrin gel. Dimension E, which is the width of the vessel channel, have to be around 400 – 1000 μm. Width of the vessel channel has to be small enough to allow the factors secreted from LF to be sufficiently delivered to EC, while large enough to allow the vessel to sufficiently grow in the fibrin gel. Dimension F is the least important in this chip. It actually does not have to be precisely controlled, although it has to be larger than 300 μm at least, to secure the vessel chamber and the single micropost in the perivascular region.

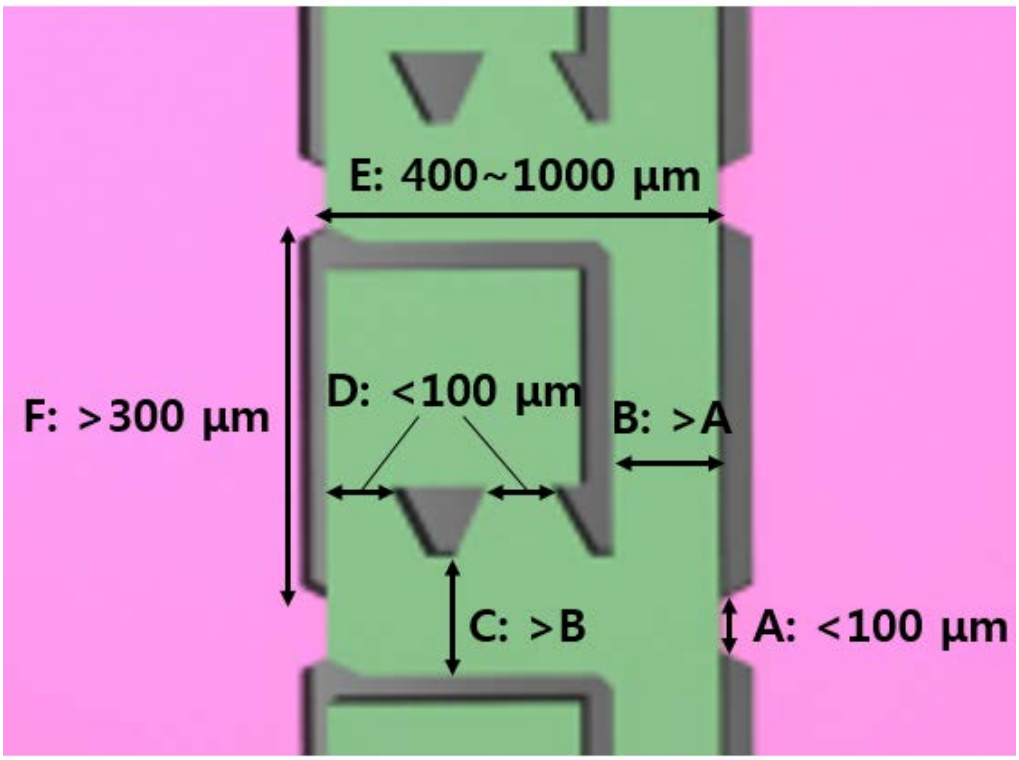

Figure 2.16 Subordinate conditions for determining dimensions of PDMS structures in the vessel channel.

Compared to the conventional permeability assay with the Transwell, which utilizes EC monolayer on the permeable membrane, this platform has several advantages. First, in the transwell assay, the endothelial cells are two dimensionally coated on the permeable membrane. However, in this platform, as shown in Fig. 2.7, the microvessels are fully lumenized with the three dimensional structure, closely mimicking the real blood vessels in our body. Second, while the endothelial cells are artificially coated on the membrane, the endothelial cells in this platform are differentiated into the microvessels by their natural angiogenic process, recapitulating the generation of the capillaries during the developmental stage of the living systems. Third, the process of the molecular diffusion across the vessel wall can be live-imaged, while in the transwell we can only perform end-point assays. This characteristic potentially allows the live imaging of other fluorescent substances like nano-particles for more detailed further studies about the vascular permeability. Lastly, this platform generates multiple microvessels simultaneously, and the permeability assay can be performed in a high-throughput manner. Summary of the comparison between this platform and the conventional Transwell assay is shown in Fig. 2.17.

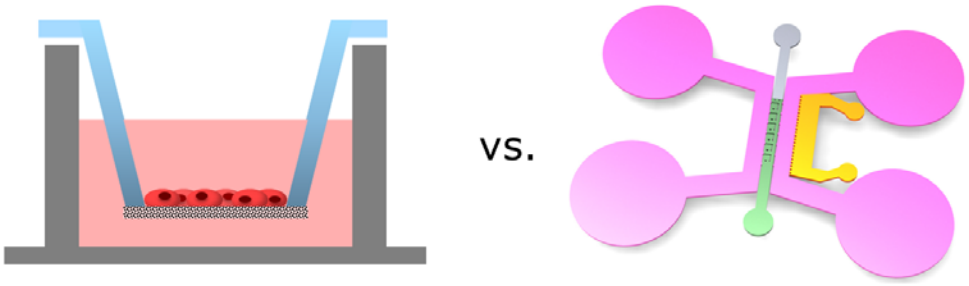

X	Three-dimensional structure	O
X	Natural angiogenic process	O
X	Molecular diffusion imaging	O
X	High-throughput screening	O

Figure 2.17 Comparison between this platform and the conventional Transwell assay.

III. DEVELOPMENT OF A MICROFLUIDIC PLATFORM FOR CANCER METASTASIS AND ANGIOGENESIS ASSAY

1. Advantage of this platform

A new chip is designed where cancer angiogenesis and transendothelial migration can be assayed in a quantitative and reproducible manner. A robust assay platform was established by forming a microvessel by vasculogenic process with spatially well-defined co-culture tumor microenvironment. The smooth boundary of the microvessel represents a close *in vivo* mimic of pre-existing blood vessel wall. Design of the chip has spatial co-culture flexibility that allows lung fibroblasts (LF) to stimulate endothelial cells to become a differentiated microvessel, followed by the cancer cell introduction at the perivascular microchannel to model the cancer-EC interactions. The endothelial cells showed an *in vivo*-like elongated morphology with proper cell–cell junctions, and the three-dimensional vascular structure opened to the media channel to allow perfusion of media into the vessel lumen. Cancer angiogenesis and blocking of the angiogenic pathway by treatment with anti-vascular endothelial growth factor (anti-VEGF; bevacizumab) was modeled successfully. Intravasation of cancer and its modulation by tumor necrosis factor-α (TNF-α) treatment was also investigated.

2. Materials and Methods

2.1 Cell culture, immunostaining, and reagents

Human umbilical vein endothelial cells (HUVEC, Lonza) were cultured in Endothelial Growth Medium (EGM-2, Lonza). Normal human lung fibroblasts (LF, Lonza) were cultured in Fibroblast Growth Medium (FGM-2, Lonza). Human glioblastoma multiforme cells, U87MG (ATCC, Virginia) were cultured in DMEM supplemented with 10% FBS, penicillin (100 U/ml) and streptomycin (100 U/ml). The MDA-MB-231 cells were obtained from ATCC (Manassas, VA). MDA-MB-231 cells were transfected with pEGFP plasmid, followed by selection of the cells with 1 mg/ml G418 (A.G. scientific, Inc.). The MDA-MB-231 GFP cells obtained from the single clone maintained in RPMI 1640 (WELGENE, Korea), supplemented with 10% FBS, 1% penicillin/streptomycin (Gibco, BRL) and 250 μg/ml G418 (A.G. scientific, Inc.). All cells were cultured in a humidified incubator at 37°C and 5% CO2.

For immunostaining, mouse monoclonal antibody specific for human ZO-1 (Alexa Fluor1594, clone ZO1-1A12, molecular probes), CD31 (AlexaFluor1647, clone WM59, BioLegends), VE-cadherin (eBioscience) and claudin-5 (Invitrogen) were used for endothelial imaging and Hoechst 33342 (molecular Probes) was used to stain the nuclei.

Bevacizumab (Avastin, Genentech) was diluted into 500 μg/ml and treated to the microvessels with the cancer introduction in the cancer angiogenesis experiments. For TNF- α treatment, recombinant Human TNF-α (PeproTech) was diluted into 5 ng/ml and treated into the microvessels starting at 24 hours before the cancer introduction.

2.2 Microfluidic device fabrication

Microfluidic devices were fabricated with the same protocol described in Chapter II. In brief, master mold of the device was fabricated by casting photo resist on a silicon wafer. Standard photo lithography protocol for SU-8 100 (Microchem, US) photoresist was used to make 150 μm thickness molds. PDMS (Dow Corning, US) was poured on the completed master mold and cured in an 80˚C dry oven for 40 minutes. The PDMS and cleaned coverslip were bonded together by using plasma treatment (Femto Science, KR). For hydrophobicity, the bonded devices were kept in dry oven with 80°C for at least 48 hours. Entire schematic drawing and detailed dimensions of the chip are shown in Fig. 3.1.

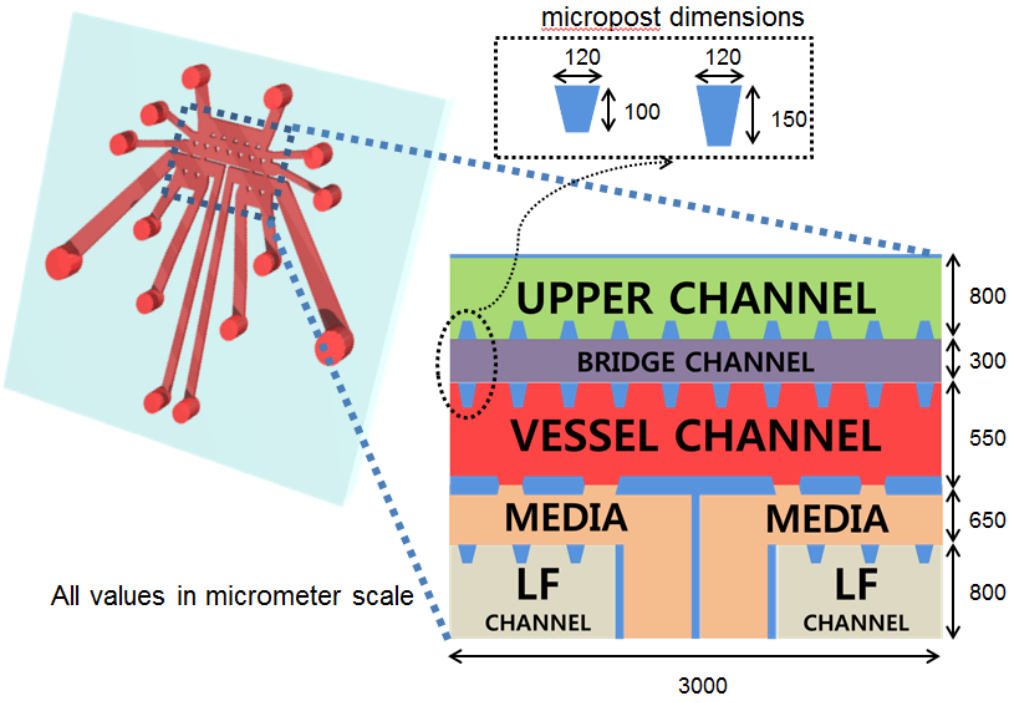

Figure 3.1 Entire schematic drawing and detailed dimensions of the chip. Seven microchannels are involved in this chip, which are partitioned with arrays of microposts. The chip was fabricated with 150 μm thickness, and punched with a sharpened 18 gauge blunt hypodermic needle for the gel injecting ports, and a 6 mm biopsy punch for media reservoirs.

2.3 Hydrogel and cell loading into the metastasis chip

HUVECs (6 million/ml in most experiments, some experiments used 3 or 9 million/ml as noted) and LFs (7 million/ml) were mixed with a fibrinogen solution (2.5 mg/ml fibrinogen with 0.15 U/ml aprotinin and 0.5 U/ml thrombin) and injected into vessel channel and LF channels, respectively (Fig. 3.2a). After incubating for two minutes to allow for fibrin polymerization, we filled EGM-2 media into the media channel. The devices were incubated for 7-8 days to engineer fully lumenized microvessel with open ends at the each media channel (Fig. 3.2b).

For cancer angiogenesis, U87MGs with fibrinogen solution were injected into the upper channel and bridge channel was filled with fibrinogen solution. For cancer intravasation, MDA-MB-231 cells (1 million/ml) were injected into the bridge channel and tilted for 40 minutes to attach to the fibrin wall between the bridge and vessel channel. For inducing chemotactic migration of the cancer cells, EBM-2 (media without additional growth factor supplements) was filled into the bridge and upper channel, while EGM-2 media was filled at the media reservoirs.

2.4 Microscopy

A confocal microscope (Olympus FV1000) was used for 3D z-stack and cross-sectional imaging. The confocal images were analyzed by IMARIS (Bitplane, Switzerland). IX81 inverted microscope (Olympus) was used for fluorescence imaging.

2.5 Data analysis

3D z-stack images were analyzed with IMARIS software. For quantifying the success rate of smooth and continuous boundary of the microvessels, the length of the vessel boundary was measured, and compared with the straight-line length of the vessel channel along the microvessel using Image J. We regarded the chip as success if the boundary length value is in a range of ± 10% to the straight-line length of the vessel channel. Every microvessels that have disconnected vessel wall was considered as failure.

Permeability coefficient calculation was performed using the same method that was presented in Chapter II. In brief, FITC-dextran solution was introduced into the microvessel and fluorescently imaged in every 15 seconds using multi-stage time-lapse mode in Metamorph. The acquired time-lapse image was analyzed with Image J and permeability coefficient was calculated based on the equation as follows:

$$P = \frac{1}{I_w} \times \frac{dI/dt}{I_i}$$

where I_w is length of the vessel wall that separates between perivascular and microvessel region, I_i is the mean intensity in the microvessel region, I is the total intensity in the perivascular region.

For the quantification of cancer angiogenesis, sprout area and the number of sprouts were manually quantified by using Image J. For quantification of cancer intravasation, the microvessels were stained with CD31 and fluorescence imaged, and cancer cells at the apical side of the microvessel were manually counted using the IMARIS software.

3. Results

3.1 Metastasis chip design

There are two previous works about the formation of a perfusable microvessel network in a microfluidic device using a co-culture system of HUVEC and LF [41, 42]. The HUVEC sprouts were stimulated by LF, which opened their lumens to both sides of the channel, allowing fluid passage through the vessels. However, the structure of microvessel network was unpredictable, and other cell types could not be introduced into the perivascular region, as the perivascular regions were filled with gel or PDMS

wall. Therefore, we generated a microvessel with more predictable geometric characteristics and with perivascular regions that could be filled with other cell types after the generation of the microvessels with vasculogenic process.

Previous design [42] produced microvessels that randomly traverse across the vessel channel. Metastasis chip was designed to establish a single microvessel with well-defined vessel wall for quantitative analysis of the cancer-EC interactions, angiogenesis and trans-endothelial migration. The chip consists of seven microchannels separated by an array of microposts following a previously described design feature [45]. The channels can be catagorized into two groups: 1) a vessel channel, two media channels, and two LF channels for microvessel formation, 2) bridge channel and upper channel for cancer introduction (Fig. 3.2a).

We used the same scheme with the previous design for generating a perfusable microvessel, which uses LF channels and a vessel channel connected by media channels to induce a paracrine interaction between LF and HUVEC. In this work, however, instead of positioning LF channels at the both side of the vessel channel as the previous design [42], the position of LF channels and two openings in the vessel channel is on the same side (lower side). This generates microvessel with two openings on the same side, while the other side of the microvessel is interfaced with another microchannel, which is called the “bridge channel” in Fig. 3.2a.

The upper and bridge channels are empty during the microvessel growth. The interface with the empty channel prevents HUVECs in the upper region of the vessel channel from migrating or generating sprouts toward the upper direction of the vessel channel, and further allows the generation of a smooth vessel wall, parallel to the interface. Cancer angiogenesis and intravasation assay could be quantitatively performed by introducing cancer cells into the empty channels.

Fig. 3.2b-d shows a schematic drawing of the generation of a microvessel, and the performance of the cancer angiogenesis and intravasation assays using the chip. We first injected an LF-fibrin mixture into the LF channels, and a HUVEC-fibrin mixture into the vessel channel to engineer the microvessel. Media was added to connect the cell-loaded channels, and a microvessel with two openings toward the media channels was generated after a 7–8-day incubation (Fig. 3.2b). Two assays were performed following the generation of the microvessel. We modeled cancer angiogenesis using the U87MG cell line, which is known for its considerable angiogenic potential [10, 58] as a cancer sprout inducer from the microvessel. We injected an U87MG-fibrin mixture into the upper channel, followed by a fibrin injection into the bridge channel (Fig. 3.2c). We observed the formation of cancer sprouts from the pre-existing microvessels toward the cancer site, which was promoted by the secretion of pro-angiogenic factors from U87MG cells. We attached MDA-MB-231 cells to the fibrin gel that was exposed to the bridge channel and supplied media to

the upper channel for the cancer intravasation assay (Fig. 3.2d). Growth factor-free media (EBM-2) was supplied at the upper channel for inducing chemotactic migration of the cancer cells toward the microvessel wall. After a 2–3-day incubation, intravasated cancer cells were observed inside the microvessels, which indicated successful modeling of the cancer intravasation process.

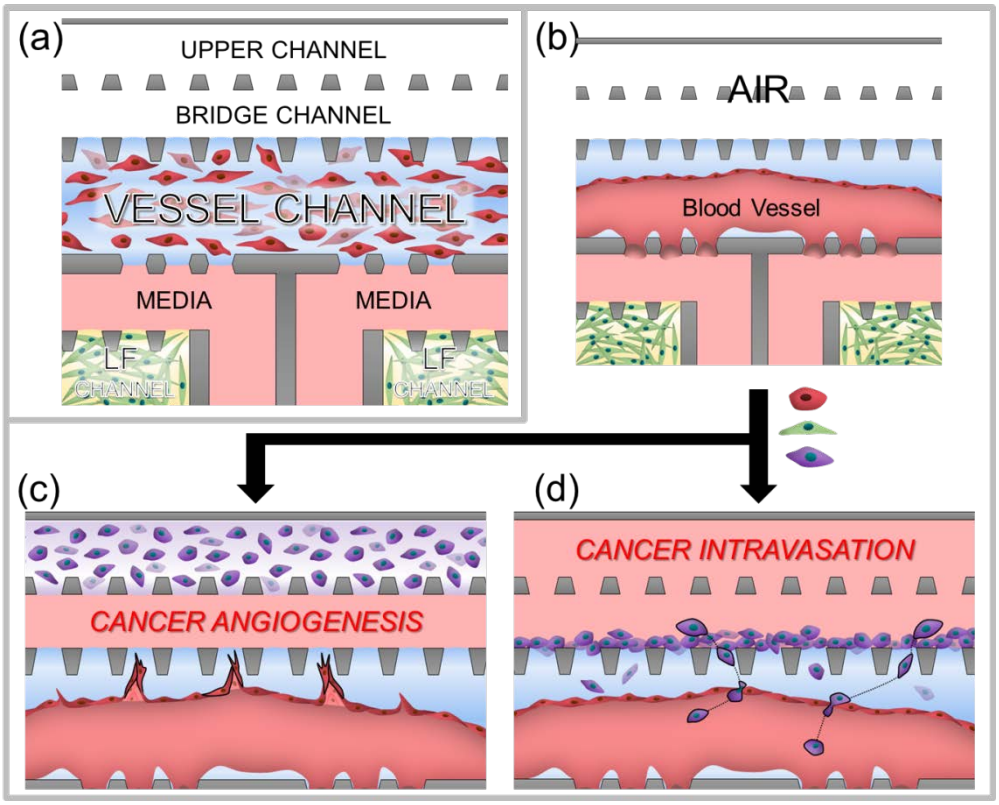

Figure 3.2 Top-down view of the metastasis chip design scheme and experimental procedures. (a) Schematic drawing of the metastasis chip. The chip consists of seven microchannels, separated by the array of microposts. LFs or HUVECs mixed with fibrinogen solution are loaded into LF and vessel channels, followed by the media injection. (b) Microvessel formation. Leaving bridge and upper channel without any fluid injection, the chip is incubated for 7–8 days for microvessel formation with three-dimensional structure. (c) For cancer angiogenesis assay, U87MGs mixed with fibrinogen solution is injected into the upper channel and fibrinogen solution is injected into the bridge

channel. Stimulated by the secretion of U87MG, angiogenic sprouts stemmed from the microvessel wall grow toward the upper channel. (d) For cancer intravasation assay, MDA-MB-231 cells are loaded into the bridge channel and tilted for their attachment on the fibrin wall. Media is filled after the attachment, and followed by several days of incubation, the MDA-MB-231 cells invade into the fibrin gel and intravasate through the microvessel wall.

3.2 Formation of perfusable microvessels with smooth and continuous boundaries

Engineering smooth and continuous vessel boundaries is necessary for quantitative analysis of angiogenesis and trans-endothelial migration. We left the bridge channel empty to minimize the generation of sprout toward the upper region of the vessel channel during the microvessel formation. Furthermore, HUVEC cell concentration has to be optimized to engineer microvessels with smooth and continuous boundaries. We tested three conditions (3, 6, and 9×10^6 HUVECs/ml and 7×10^6 LF/ml) using 4–5 chips per condition, and results are expressed as the mean of three independent experiments. Fig. 3.3a shows the microvessel morphology on day 7 under each condition. The microvessel boundary was strongly dependent on the HUVEC concentration. Microvessels formed with 3×10^6 HUVECs /ml showed a rough and discontinuous boundary with the scattered small sprouts, and the microvessel was not perfusable.

Microvessels formed with 9×10^6 HUVECs /ml had a continuous boundary with fewer, scattered, small sprouts. However, the microvessels covered the majority of the area between the microposts at the upper region and exhibited a ‘rough’ boundary. In contrast, microvessels formed with 6×10^6 HUVECs /ml was perfusable, and showed not only a continuous boundary

without scattered small sprouts but also the smoothest boundary morphology with few sprouts protruding toward the upper region of the vessel channel.

Fig. 3.3b shows the success rate for microvessel formation for different HUVEC concentrations. Using 6×10^6 HUVECs/ml resulted in the highest success rate (~77%) in terms of obtaining smooth and continuous boundary morphology. Therefore, we concluded that the microvessels formed using 6×10^6 HUVECs/ml showed the most pertinent boundary morphology for our goal, and this condition was used in all further experiments.

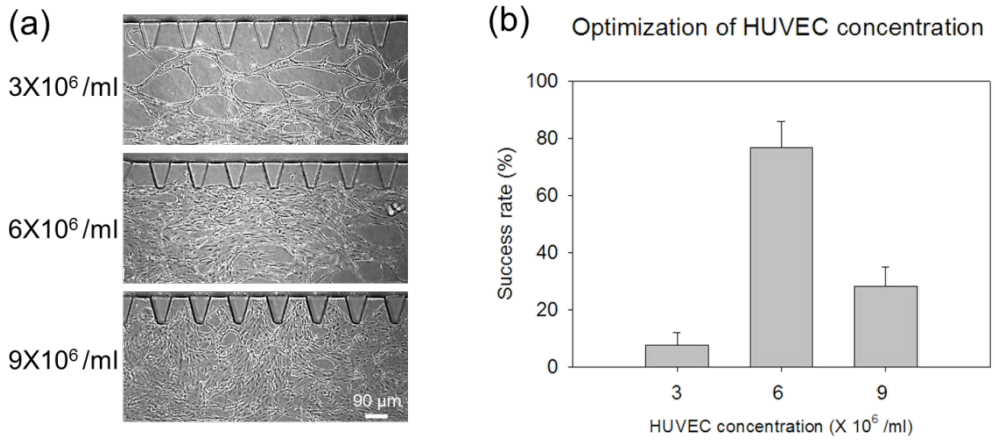

Figure 3.3 HUVEC concentration optimization for generating smooth and continuous vessel boundary. (a) Micrograph of the microvessels according to the initial HUVEC concentration at day 7. HUVEC concentration 6×10^6 /ml shows the smoothest and continuous microvessel wall. (b) Success rate of the smooth microvessel wall formation. HUVEC concentration 6×10^6 /ml shows the highest success rate of the smooth vessel wall formation.

Fig. 3.4 shows a series of micrographs during the microvessel formation using 6×10^6 HUVECs/ml condition. The HUVECs began to exhibit an elongated morphology with the small vacuoles 2 days after the seeding. At this time, the microvessels were not fully connected and no patent lumen was observed. HUVECs began to form a continuous lumen by day 4. The vessels began to merge to form a single continuous microvessel in the vessel channel. Furthermore, HUVECs in the upper region between the microposts began to migrate toward the lower direction, forming a flat and smooth microvessel boundary. The vessels fused to yield one fully lumenized microvessel by day 7, and HUVECs in the upper region between the microposts had migrated lower compared to those on day 4 to form the smooth microvessel boundary. The microvessel maintained its morphological characteristics for $\geq$ 14 days without a regression.

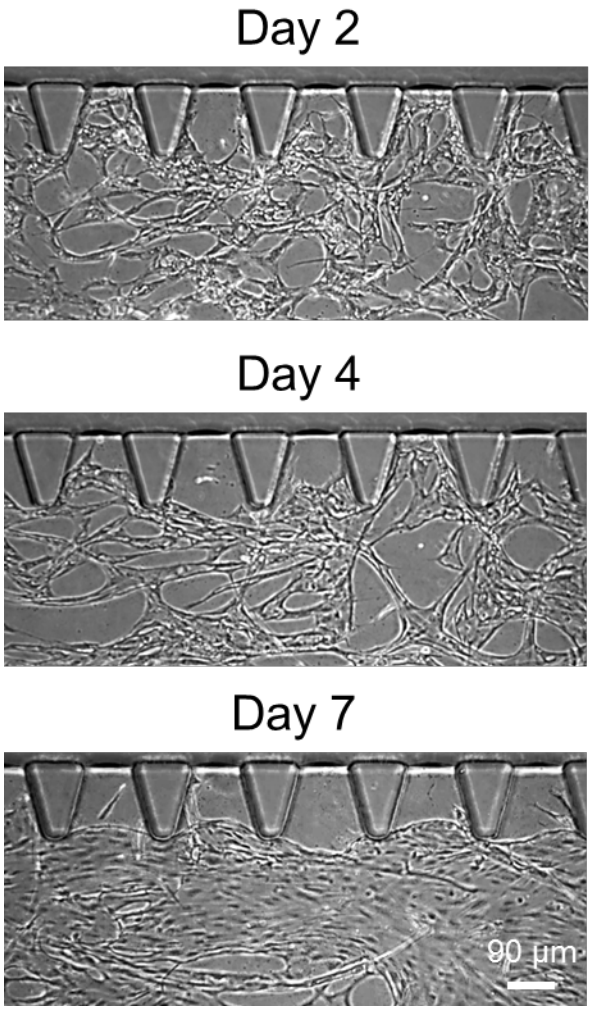

Figure 3.4 Time-lapse micrograph of the microvessel formation in 6×10^6 /ml HUVEC concentration. Endothelial cells scattered in the vessel channel fuse together and become a microvessel with patent, perfusable lumen. Furthermore, endothelial cells at the region between upper microposts gradually migrate toward the lower region, and form smooth and continuous microvessel wall at day 7.

3.3 Characterization of the microvessel

After the formation of the microvessel in day 7, CD31 (red) and nuclei (blue) were immunostained and imaged with a confocal microscope (Fig. 3.5). Cross-sectional images of the microvessel at various positions revealed continuous patent three-dimensional lumens. The microvessel was composed of a clear lumen that connected both openings toward the media channels. To test the vessel integrity and continuity of the lumen, we introduced microbeads through the vessels. We confirmed that ~94% (101 of 108 chips) of the microvessels opened toward the media channels and could be perfused.

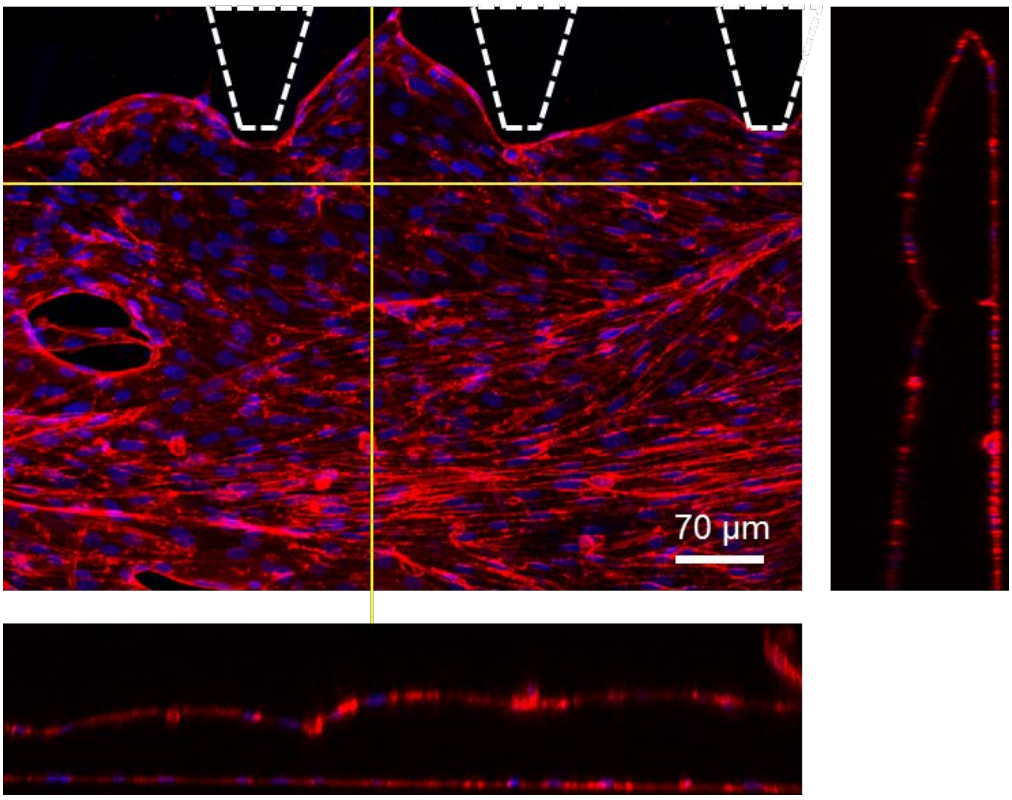

Figure 3.5 Geometric characterization of the fully developed microvessel. 3D projection and cross-sectional image of the microvessel shows patent lumen formation inside the microvessel in day 7.

We introduced FITC-dextran solution (20 kDa) into the microvessel to verify the patency of the lumen, and visualized their behavior using a fluorescence microscopy. The FITC-dextran filled the microvessel lumen without severe focal leakage through the wall (Fig. 3.6). The permeability coefficient of the microvessel was $1.58 \pm 0.32 \times 10{-}6$cm/s (mean ± standard error, n = 5) as determined by a time-lapse acquisition of the FITC-dextran intensity profile. The permeability coefficient was in the range of those for other in vitro models of blood vessels [13, 36, 51], indicating that the microvessel expresses the appropriate cell–cell junctions.

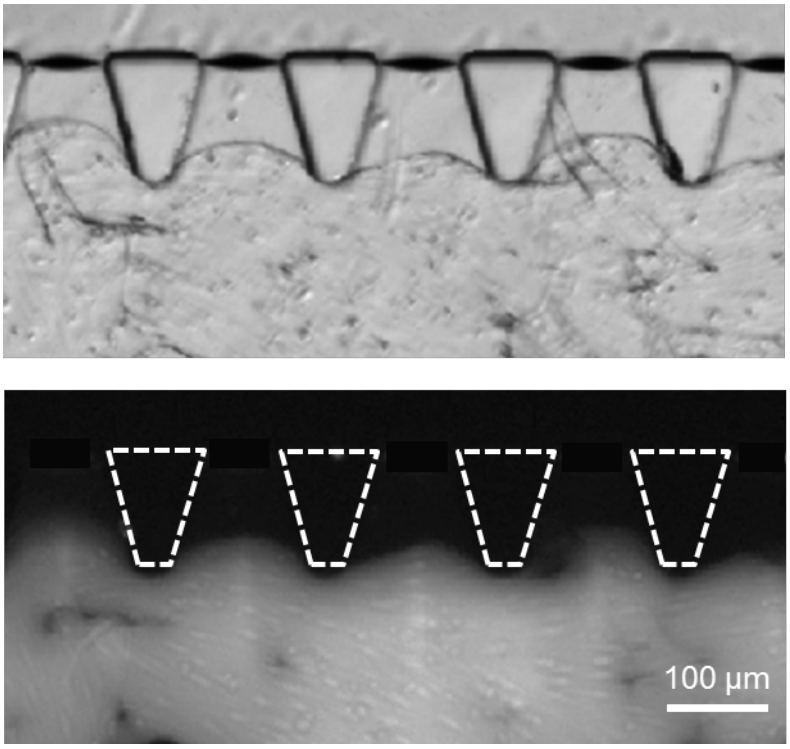

Figure 3.6 DIC Micrograph of the microvessel wall and fluorescence micrograph of the same region with the introduction of 20 kDa FITC-dextran into the lumen. The fluorescence micrograph shows FITC-dextran containing microvessel without severe leakage at the vessel wall, showing the pertinent function of cell-cell junction. The experiment was performed with microvessels in day 7.

We further analyzed the junctions by fluorescent immunostaining for claudin-5 and ZO-1 (Fig. 3.7a, b). The fluorescence images of two cell–cell junctions showed a smooth, clear elongated morphology without any disrupted or wrinkled positions, which are the basic characteristics of cell–cell junctions in normal blood vessels in vivo. We confirmed that the microvessels formed in this chip exhibited the cell–cell junctions similar to those in vivo, based on the permeability measurements and imaging of the junctions.

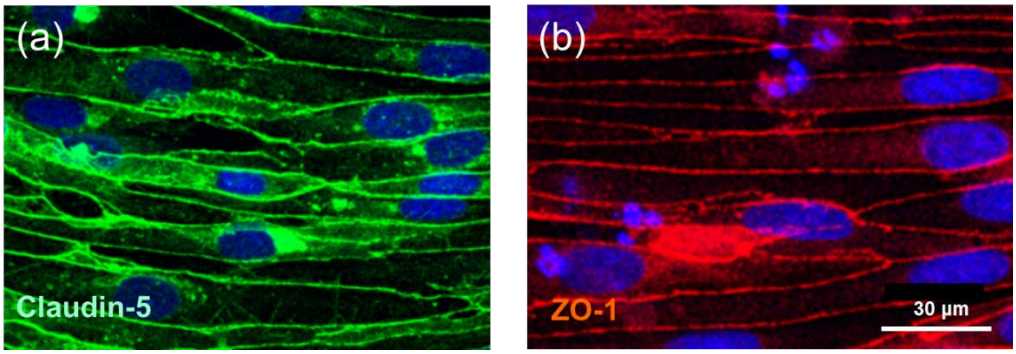

Figure 3.7 Junctional images of microvessel in day 7. Smooth and clear lines with elongated morphology of Claudin-5 and ZO-1 without rinkled or disrupted region show pertinent junctional expressions similar to that *in vivo*.

3.4 Cancer angiogenesis assay

We analyzed the angiogenic potential of cancer cells by using the microvessels with a smooth vessel wall. After formation of the microvessels in the channel (day 7–8), we introduced U87MG, a glioblastoma cell line with high angiogenic potential, and a fibrin mixture into the upper channel, while the bridge channel was filled with fibrin gel only. We regarded the microvessel as that pre-existing at the cancer site, whereas the U87MG cells in the perivascular region secrete angiogenic factors to induce production of angiogenic sprouts toward the microvessels. We tested three different conditions at the upper channel: Only fibrin gel without cell as a control, and 5×10^6 U87MG /ml with or without bevacizumab (bev), which is an anti-VEGF antibody used widely for targeting angiogenesis. We analyzed the angiogenic sprouting from the microvessels and calculated the mean values of six chips per condition.

Three days after introduction of U87MG cells into the chip, we imaged the microvessels and quantified the number and coverage area of angiogenic sprouts under each condition. As shown in Fig. 3.8, most of the microvessels without U87MG cells showed few angiogenic sprouts, Furthermore, most microvessels treated with bevacizumab had a flat boundary without angiogenic sprouts. In some bevacizumab-treated samples, we observed sprout regression which existed prior to introduction of cancer cells and bevacizumab (Fig. 3.8).

We postulate that this was due to the anti-angiogenic effect of bevacizumab; however, a more in-depth analysis is required. Compared to these results, microvessels with U87MG cells showed a significant number of angiogenic sprouts (Fig. 3.9). Enlarged three-dimensional confocal image of the vessel sprouts shows clear sprout formations from the vessel wall.

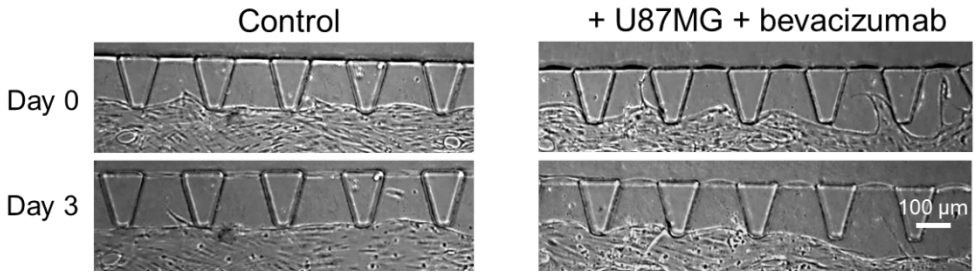

Figure 3.8 Comparison of the microvessel wall before and three days in control experiment, and the cancer injection with bevacizumab treatment. No significant angiogenic sprouts are seen for both conditions.

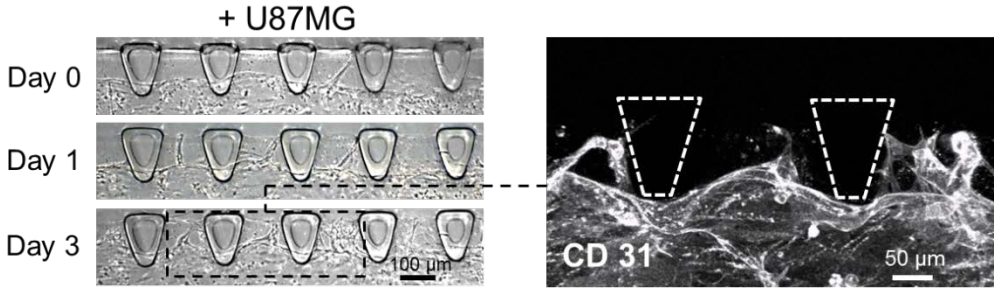

Figure 3.9 Comparison of the microvessel wall before and three days after the cancer injection. Angiogenic sprouts from the microvessel wall are formed toward the upper channel, stimulated by the secretion of cancer cells. 3D confocal image (CD31) also clearly shows the angiogenic sprouts stimulated by the cancer secretion.

We next quantified the number and coverage area of sprouts. The microvessels with cancer cells exhibited markedly increased sprout numbers and coverage areas compared to the control (Fig. 3.10). Furthermore, bevacizumab treatment attenuated the angiogenic potential of the U87MG cells, drastically decreasing the number and coverage area of the microvessel sprouts. These trends of the sprout induction by cancer cells and sprout attenuation by anti-VEGF treatment are in agreement with previous in vivo reports [10, 67], and demonstrate that this microvessel model is appropriate for the assessment of drugs targeting cancer angiogenesis.

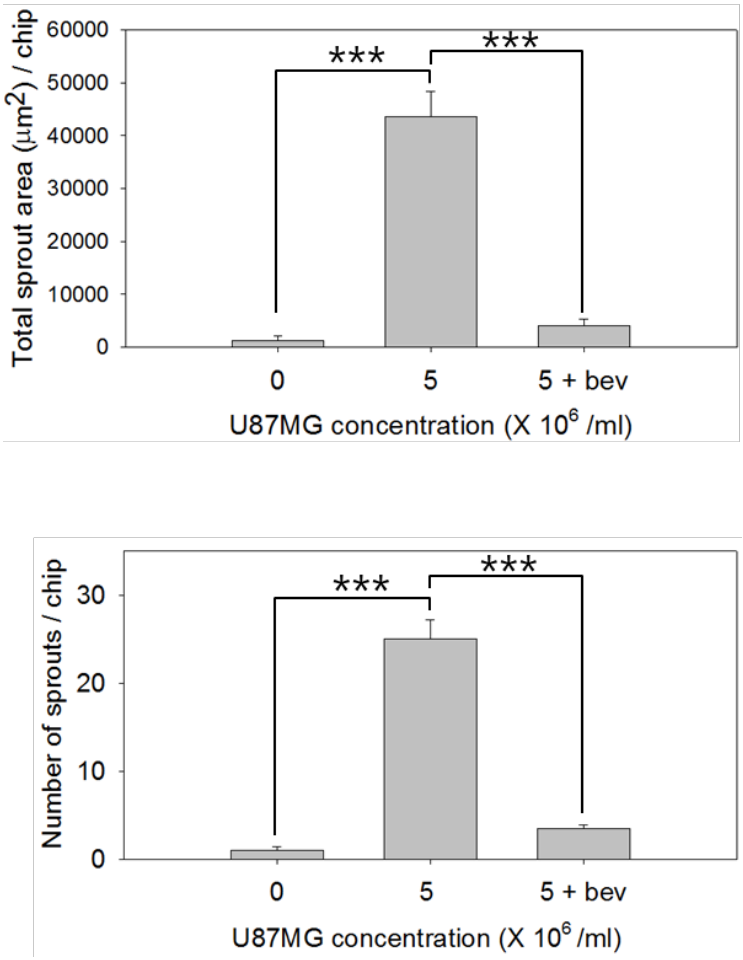

Figure 3.10 Quantification of coverage area and numbers of sprouts. Cancer cells induce significant amount of sprouts from the microvessel, and bevacizumab treatment drastically reduces the coverage area and the number of cancer sprouts, showing the anti-angiogenic potential of the bevacizumab for the cancer therapy (***$p<0.0005$). Two independent experimenters performed the counting for the data in the graphs. Error bars represent SEM.

3.5 Cancer intravsation assay

We next used the microvessel as a pre-existing blood vessel for assessment of transendothelial migration of MDA-MB-231, an aggressive metastatic breast cancer cell line [27, 51, 68]. As shown in Fig. 3.2d, cancer cells attached to the interface between the fibrin gel and bridge channel, and were incubated for 2–3 days to allow them to migrate toward and penetrate into the microvessels. Growth factor-free media (EBM-2) was introduced in the upper channel during the incubation to induce chemotactic migration of the cancer cells toward the microvessel. Fig. 3.11 shows fluorescence and differential interference contrast micrographs of a MDA-MB-231 cancer cell (green) in the process of intravasation through the microvessel wall (red).

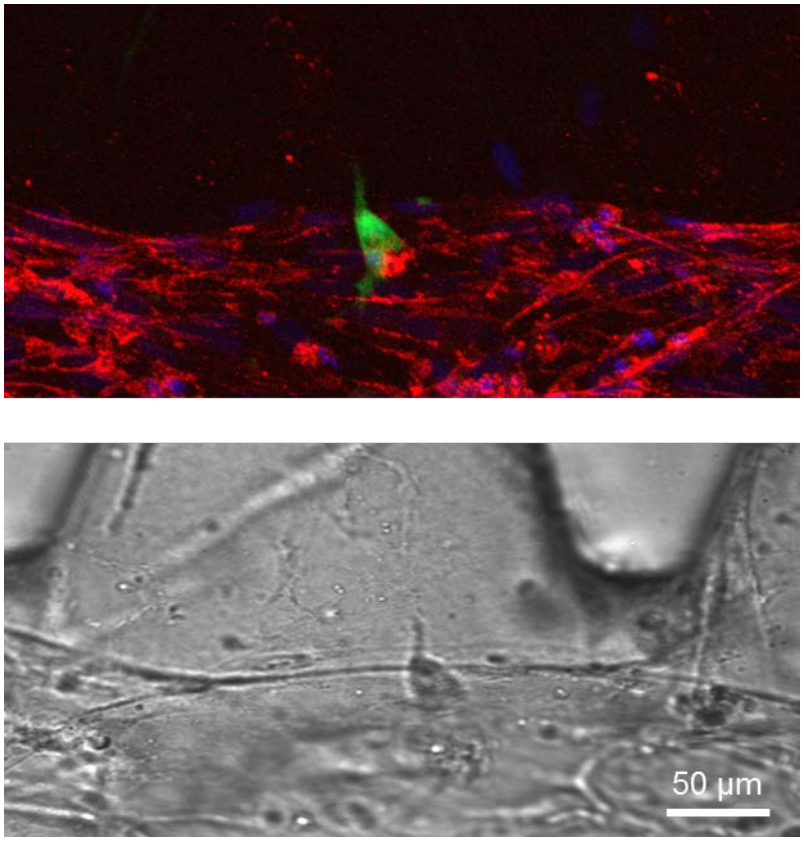

Figure 3.11 Micrographs of a cancer cell trans-migrating through the microvessel wall. (Red: CD31, Green: MDA-MB-231, and Blue: Nuclei) Fluorescence and DIC micrographs show that the cancer cell is embedded into the microvessel wall.

Fig. 3.12a shows a fluorescence and differential interference contrast micrograph of a MDA-MB-231 cancer cell (green) in the process of migration toward the microvessel wall. The image was acquired at one day after the cancer introduction into the bridge channel. After incubating for three days, we could see several intravasated cancer cells into the vessel lumen. We performed three-dimensional imaging of the microvessel with an intravasated cancer cell. The cross-sectional images clearly show the intravasated cancer cell that is attaching its body on the inside of the vessel wall (Fig. 3.12b). We manually counted the number of cancer cells intravasated into the microvessels by analyzing three-dimensional images at day 3.

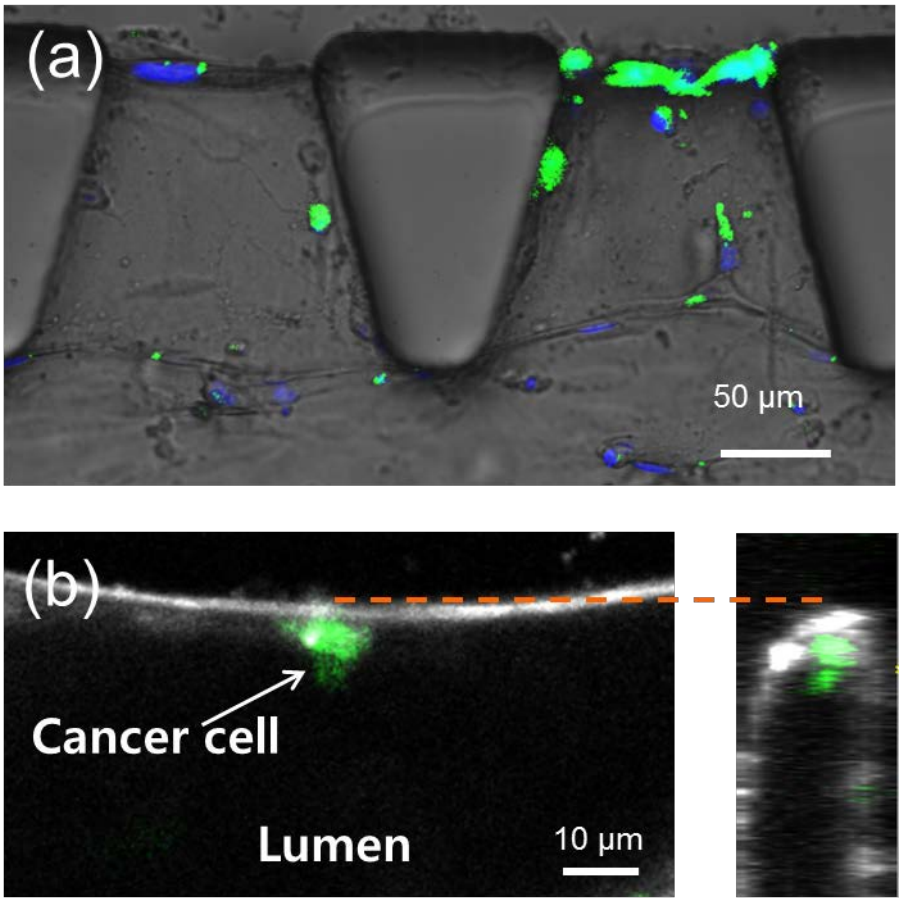

Figure 3.12 Micrograph of the cancer intravasation. (a) Micrograph of cancer cells migrating toward the microvessel wall (Green: MDA-MB-231 and Blue: Nuclei). The image was acquired two days after the cancer introduction into the bridge channel. (b) The cross-sectional images clearly show the cancer cell intravasated through the vessel wall and located in the vessel lumen (White: CD31 and Green: MDA-MB-231).

In this assay, the microvessels were treated with 5 ng/ml TNF-α 24 h before the introduction of the cancer cells, and compared the rate of cancer intravasation to that of the control. We first determined the effect of TNF-α on junctional expression by endothelial cells. The adherens junction VE-cadherin in the TNF-α treated microvessels exhibited disrupted continuity and wrinkled morphology compared to control microvessels (Fig. 3.13a,b). The permeability of TNF-α–treated microvessels over 24 h was $2.22 \pm 0.67 \times 10^{-6}$ cm/s, (mean ± standard error, n = 5 chips), which was ~1.4-fold higher than under the normal condition. These results confirm the effect of TNF-α on junctional disruption of endothelial cells, and are in agreement with previous reports [52, 53, 55].

We further analyzed the effect of TNF-α on cancer cell intravasation. We compared the rate of intravasation with or without TNF-α treatment, (n = 7 chips per condition). The rate of cancer intravasation of TNF-α-treated microvessels was ~3-fold higher than that of the control (Fig. 3.13c). This suggests that TNF-α treatment exerted marked effects on cancer cell intravasation, in agreement with previous reports [69-71].

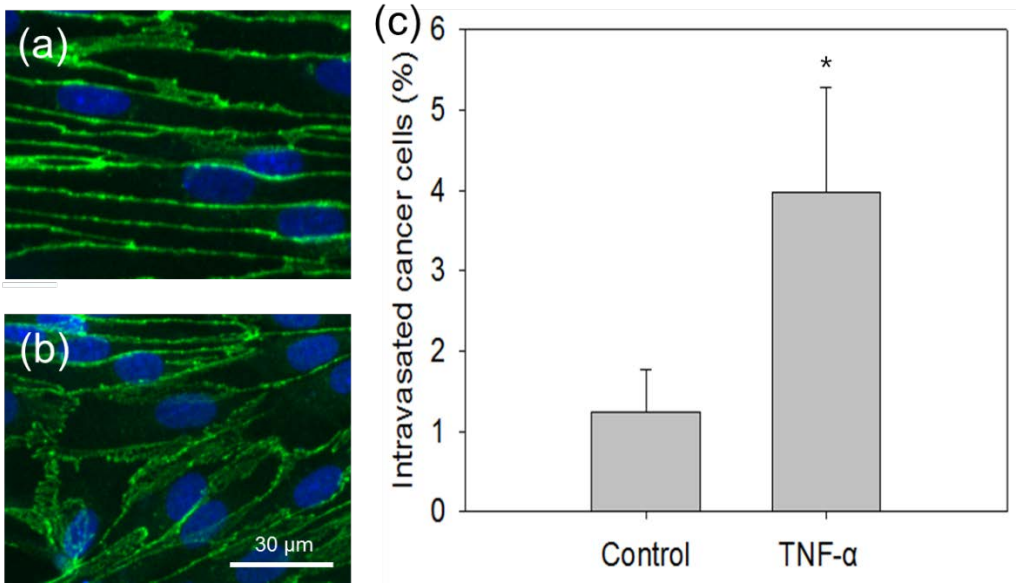

Figure 3.13 Micrograph of the VE-Cadherin expressed at the cell-to-cell junction in the microvessel. Compared to the microvessels in normal condition (a), VE-cadherin in TNF-a treated microvessel shows disrupted and wrinkled morphology (b), showing the junctional disruption by the effect of TNF-a. (c) Comparison of the intravasation rate between control and TNF-a treated microvessel. Compared to the control experiment, TNF-a treated microvessel showed a significantly higher rate of cancer intravasation, showing the effect of the TNF-a to the junctional function of the microvessel and cancer intravasation (*$p<0.05$ compared to control). Error bars represent SEM.

4. Discussion

We developed a microfluidic chip for assays of cancer angiogenesis and intravasation. Many previous angiogenesis or intravasation assays use an endothelial monolayer attached to a hydrogel or porous membrane [34, 36, 71]. Our assay involves use of a microvessel formed by natural vasculogenic processes as a pre-existing vessel for cancer cells; thus the model mimics the *in vivo* conditions with higher similarity.

This chip design has two main advantages over previous chips developed by our group regarding vascular structural engineering [41, 42]. First, this chip facilitated introduction of diverse cell types into the perivascular region after formation of microvessels in the vessel channel. This was achieved by locating LF channels on the same side (lower region), while the upper region was exposed to an empty channel, which was filled with other cell types after formation of the microvessels. Second, this chip resulted in generation of a smooth and continuous vessel boundary, which is important for further research. If the vessel boundary is overly bumpy and complex, analysis of the cancer angiogenesis and intravasation data would be laborious and inaccurate. Furthermore, when sprout tips remained at the vessel wall, as under the 3×10^6/ml condition (Fig. 3.3a), occasional focal leakage occurred at the tip, which indicated loose cell-to-cell junctions. This may also affect the results of experiments.

The mechanism underlying the generation of a smooth and continuous vessel boundary was not determined in this study. However, we identified two key factors for generating a smooth and continuous vessel boundary. First, the channel that contacts the vessel boundary should not be filled with gel or media. The bridge channel must contain only air during microvessel growth. This prevents the generation of growth factor gradients from the bridge channel, and prevents most of the endothelial cells from migrating or generating sprouts toward that empty channel. At the same time, media is supplied from the media channels, which led to migration of the endothelial cells toward the lower region, closer to the media channels. Therefore, the endothelial cells at the gap between microposts tend to migrate toward the lower direction and form a smooth vessel boundary (Fig. 3.4).

Second, optimizing the HUVEC concentration was important for generating a smooth vessel boundary. A smooth boundary was not formed at low HUVEC concentrations. As under the 3×10^6/ml condition (Fig. 3.3a), endothelial cells formed a thicker vessel in the lower region, whereas they were scarce in the upper region of the vessel channel. We speculated that this was due to migration of endothelial cells toward the media supply, and cells in the upper region of the vessel channel became scarce because the number of endothelial cells was insufficient to fill the vessel channel from the lower to the upper region. In contrast, if the HUVEC concentration was too high, excess endothelial cells were present in the vessel channel, which inhibited migration

of endothelial cells and generation of a smooth vessel boundary, as under the 9×10^6 /ml condition (Fig. 3.3a). Therefore, the optimal HUVEC concentration was 6×10^6/ml, which was used in all experiments.

The system described in this work shows promising junctional characteristics with pertinent three dimensionality. However, there are several potential limitations in terms of physiological similarity to the blood vessels *in vivo*. Although the geometry that locates stromal cells at the lower side allows straight and smooth vessel boundary, there could be non-physiologic gradient of growth factors secreted from LF, through the width of the vessel channel during the vessel maturation. The HUVECs that are close to the media channels will be sufficiently supplied by the growth factors, while the HUVECs located far from the media channels could not be. They will be equally supplied by the factors after the vessel opens their lumen to the media channels, but the non-physiological gradient formation during the vessel maturation can affect the physiological characteristics of the microvessels. Furthermore, the microvessels were solely grown without pericytes or smooth muscle cells, which contribute to the stabilization and normal function of capillaries and larger venules, respectively.

To demonstrate the utility of the metastasis chip, we established two assays using microvessels generated by natural vasculogenic process. Cancer angiogenesis and its inhibition by the treatment of anti-VEGF (bevacizumab)

were successfully reproduced. Cancer intravasation, together with its modulation by the treatment of TNF-α, was also recreated using this model. Although further investigation is required, we speculate that this model will facilitate investigation of cancer angiogenesis and intravasation due to its use of a more realistic method of generating the vascular structure, whereas other models use an artificial coating of endothelial cells on a hydrogel or porous membrane. Comparing this system with other pre-established in vitro models with deeper biology will be a topic for future investigations.

IV. CONCLUSION

Two simple and robust experimental platforms were described for *in vitro* vascular biology assays. For vascular permeability assay, a novel microfluidic design was developed to form multiple perfusable 3D microvessels. The microvessels were formed by a natural angiogenic process and exhibit reliable functional barrier properties. Presence and detailed arrangement of several components of cell-cell junctions (Claudin-5, VE-cadherin, and ZO-1) were confirmed by immunohistochemistry. The vessels acquired barrier function similar to those measured *in vivo* experiments with relatively low permeability coefficients for *in vitro* measurements. Permeability coefficient of 1.55×10^{-6} cm/s was obtained with 70 kD FITC-dextran, which is in the range of previously reported values for *in vitro* measurements. Showing a similar trend with previous reports, the vessels showed decreased permeability with increasing molecular weight of FITC-Dextran (7.33×10^{-6} cm/s for 4 KD to 1.55×10^{-6} cm/s for 70 kD). Manipulation of barrier properties by addition of agonists and growth factors was demonstrated. We further validated the model by generating tumor-associated microvessels and observed normalization of hyperpermeability when treated with anti-VEGF antibody, bevacizumab. This result is consistent with the mechanism of action for bevacizumab.

For cancer angiogenesis and intravasation assay, a novel microfluidic design was developed to form a perfusable 3D microvessel with empty perivascular region. The microvessels were formed by a natural vasculogenic process and exhibit reliable functional barrier properties. The cell concentration was optimized to generate microvessel with smooth vessel boundaries. For cancer angiogenesis assay, U87MG cancer cell line was introduced at the perivascular region. The cancer sprouts were observed three days after the cancer introduction, and could be attenuated by the treatment of anti-VEGF, bevacizumab. For cancer intravasation assay, MDA-MB-231 cancer cell line was introduced into the perivascular region and their migration toward the vessel wall was observed. Treatment of TNF-α showed disrupted morphology of the vessel junctions and increased portion of the intravasated cancer cells, agreeing with the previous *in vivo* studies.

The models have potential to be applied for various studies, including cancer cell or leukocyte extravasation, mechanotransduction of endothelial cells to the intraluminal flow. The robustness and reproducibility of these microfluidic chip-based microvessels, combined with the feasibility for flexible customizable chip design, promise to make it a versatile device for future investigations in fundamental vascular biology as well as drug screening.

Bibliography

[1] Ito, A., S. Hirota, H. Mizuno, Y. Kawasaki, T. Takemura, T. Nishiura, Y. Kanakura, Y. Katayama, S. Nomura, and Y. Kitamura, *Expression of vascular permeability factor (VPFNEGF) messenger RNA by plasma cells: Possible involvement in the development of edema in chronic inflammation.* Pathology international, 1995. **45**(10): p. 715-720.

[2] McDONALD, D.M., *Angiogenesis and remodeling of airway vasculature in chronic inflammation.* American journal of respiratory and critical care medicine, 2001. **164**(supplement_2): p. S39-S45.

[3] Druey, K.M. and P.R. Greipp, *Narrative review: the systemic capillary leak syndrome.* Annals of internal medicine, 2010. **153**(2): p. 90-98.

[4] Beller, T.C., A. Maekawa, D.S. Friend, K.F. Austen, and Y. Kanaoka, *Targeted gene disruption reveals the role of the cysteinyl leukotriene 2 receptor in increased vascular permeability and in bleomycin-induced pulmonary fibrosis in mice.* Journal of Biological Chemistry, 2004. **279**(44): p. 46129-46134.

[5] Bergers, G. and L.E. Benjamin, *Tumorigenesis and the angiogenic switch.* Nature Reviews Cancer, 2003. **3**(6): p. 401-410.

[6] Carmeliet, P. and R.K. Jain, *Angiogenesis in cancer and other diseases.* nature, 2000. **407**(6801): p. 249-257.

[7] Sahai, E., *Illuminating the metastatic process.* Nature Reviews Cancer, 2007. **7**(10): p. 737-749.

[8] Nagy, J.A., L. Benjamin, H. Zeng, A.M. Dvorak, and H.F. Dvorak, *Vascular permeability, vascular hyperpermeability and angiogenesis.* Angiogenesis, 2008. **11**(2): p. 109-119.

[9] Gerlowski, L.E. and R.K. Jain, *Microvascular permeability of normal and neoplastic tissues.* Microvascular research, 1986. **31**(3): p. 288-305.

[10] Yuan, F., Y. Chen, M. Dellian, N. Safabakhsh, N. Ferrara, and R.K. Jain, *Time-dependent vascular regression and permeability changes in established human tumor xenografts induced by an anti-vascular endothelial growth factor/vascular permeability factor antibody.* Proceedings of the National Academy of Sciences, 1996. **93**(25): p. 14765-14770.

[11] Yuan, W., Y. Lv, M. Zeng, and B.M. Fu, *Non-invasive measurement of solute permeability in cerebral microvessels of the rat.* Microvascular research, 2009. **77**(2): p. 166-173.

[12] Jacobs, M. and M. Levin, *An improved endothelial barrier model to*

investigate dengue haemorrhagic fever. Journal of Virological Methods, 2002. **104**(2): p. 173-185.

[13] Kazakoff, P., T. McGuire, E. Hoie, M. Cano, and P. Iversen, *Anin vitro model for endothelial permeability: Assessment of monolayer integrity.* In Vitro Cellular & Developmental Biology - Animal, 1995. **31**(11): p. 846-852.

[14] Martins-Green, M., M. Petreaca, and M. Yao, *Chapter 8 An Assay System for In Vitro Detection of Permeability in Human "Endothelium"*, in *Methods in Enzymology*, A.C. David, Editor. 2008, Academic Press. p. 137-153.

[15] Michel, C.C. and F.E. Curry, *Microvascular Permeability.* Physiological Reviews, 1999. **79**(3): p. 703-761.

[16] Nevo, N., N. Chossat, W. Gosgnach, D. Logeart, J.-J. Mercadier, and J.-B. Michel, *Increasing endothelial cell permeability improves the efficiency of myocyte adenoviral vector infection.* The Journal of Gene Medicine, 2001. **3**(1): p. 42-50.

[17] Booth, R. and H. Kim, *Characterization of a microfluidic in vitro model of the blood-brain barrier ([small mu]BBB).* Lab on a Chip, 2012. **12**(10): p. 1784-1792.

[18] Griep, L.M., F. Wolbers, B. Wagenaar, P.M. Braak, B.B. Weksler, I.A. Romero, P.O. Couraud, I. Vermes, A.D. Meer, and A. Berg, *BBB ON CHIP: microfluidic platform to mechanically and biochemically modulate blood-brain barrier function.* Biomedical Microdevices, 2013. **15**(1): p. 145-150.

[19] Ma, S.H., L.A. Lepak, R.J. Hussain, W. Shain, and M.L. Shuler, *An endothelial and astrocyte co-culture model of the blood-brain barrier utilizing an ultra-thin, nanofabricated silicon nitride membrane.* Lab on a Chip, 2005. **5**(1): p. 74-85.

[20] Li, G., M. Simon, L. Cancel, Z.-D. Shi, X. Ji, J. Tarbell, B. Morrison, III, and B. Fu, *Permeability of Endothelial and Astrocyte Cocultures: In Vitro Blood–Brain Barrier Models for Drug Delivery Studies.* Annals of Biomedical Engineering, 2010. **38**(8): p. 2499-2511.

[21] Nakagawa, S., M.A. Deli, H. Kawaguchi, T. Shimizudani, T. Shimono, Á. Kittel, K. Tanaka, and M. Niwa, *A new blood–brain barrier model using primary rat brain endothelial cells, pericytes and astrocytes.* Neurochemistry International, 2009. **54**(3–4): p. 253-263.

[22] Tsujii, M., S. Kawano, S. Tsuji, H. Sawaoka, M. Hori, and R.N. DuBois, *Cyclooxygenase regulates angiogenesis induced by colon cancer cells.* cell, 1998. **93**(5): p. 705-716.

[23] Abdollahi, A., D.W. Griggs, H. Zieher, A. Roth, K.E. Lipson, R. Saffrich, H.-J. Gröne, D.E. Hallahan, R.A. Reisfeld, and J. Debus, *Inhibition of αvβ3 integrin survival signaling enhances antiangiogenic and antitumor effects of radiotherapy.* Clinical Cancer Research, 2005. **11**(17): p. 6270-6279.

[24] Jin, F., U. Brockmeier, F. Otterbach, and E. Metzen, *New insight into the SDF-1/CXCR4 axis in a breast carcinoma model: hypoxia-induced endothelial SDF-1 and tumor cell CXCR4 are required for tumor cell intravasation.* Molecular Cancer Research, 2012. **10**(8): p. 1021-1031.

[25] Kramer, R.H. and G.L. Nicolson, *Interactions of tumor cells with vascular endothelial cell monolayers: a model for metastatic invasion.* Proceedings of the National Academy of Sciences, 1979. **76**(11): p. 5704-5708.

[26] Kusama, T., M. Mukai, M. Tatsuta, H. Nakamura, and M. Inoue, *Inhibition of transendothelial migration and invasion of human breast cancer cells by preventing geranylgeranylation of Rho.* International journal of oncology, 2006. **29**(1): p. 217-223.

[27] Lee, T.-H., H.K. Avraham, S. Jiang, and S. Avraham, *Vascular endothelial growth factor modulates the transendothelial migration of MDA-MB-231 breast cancer cells through regulation of brain microvascular endothelial cell permeability.* Journal of Biological Chemistry, 2003. **278**(7): p. 5277-5284.

[28] Roetger, A., A. Merschjann, T. Dittmar, C. Jackisch, A. Barnekow, and B. Brandt, *Selection of Potentially Metastatic Subpopulations Expressing c-< i> erb</i> B-2 from Breast Cancer Tissue by Use of an Extravasation Model.* The American journal of pathology, 1998. **153**(6): p. 1797-1806.

[29] Zabel, B.A., S. Lewén, R.D. Berahovich, J.C. Jaén, and T.J. Schall, *The novel chemokine receptor CXCR7 regulates trans-endothelial migration of cancer cells.* Mol Cancer, 2011. **10**(73): p. 10.1158.

[30] Anderson, J.R., D.T. Chiu, H. Wu, O.J. Schueller, and G.M. Whitesides, *Fabrication of microfluidic systems in poly (dimethylsiloxane).* Electrophoresis, 2000. **21**: p. 27-40.

[31] Chung, S., R. Sudo, V. Vickerman, I.K. Zervantonakis, and R.D. Kamm, *Microfluidic platforms for studies of angiogenesis, cell migration, and cell–cell interactions.* Annals of biomedical engineering, 2010. **38**(3): p. 1164-1177.

[32] Lee, H., M. Chung, and N.L. Jeon, *Microvasculature: An essential component for organ-on-chip systems.* MRS Bulletin, 2014. **39**(01): p.

51-59.
[33] Chrobak, K.M., D.R. Potter, and J. Tien, *Formation of perfused, functional microvascular tubes in vitro.* Microvascular research, 2006. **71**(3): p. 185-196.
[34] Bischel, L.L., E.W. Young, B.R. Mader, and D.J. Beebe, *Tubeless microfluidic angiogenesis assay with three-dimensional endothelial-lined microvessels.* Biomaterials, 2013. **34**(5): p. 1471-1477.
[35] Walker, G.M. and D.J. Beebe, *A passive pumping method for microfluidic devices.* Lab on a Chip, 2002. **2**(3): p. 131-134.
[36] Zheng, Y., J. Chen, M. Craven, N.W. Choi, S. Totorica, A. Diaz-Santana, P. Kermani, B. Hempstead, C. Fischbach-Teschl, and J.A. López, *In vitro microvessels for the study of angiogenesis and thrombosis.* Proceedings of the National Academy of Sciences, 2012. **109**(24): p. 9342-9347.
[37] Miller, J.S., K.R. Stevens, M.T. Yang, B.M. Baker, D.-H.T. Nguyen, D.M. Cohen, E. Toro, A.A. Chen, P.A. Galie, and X. Yu, *Rapid casting of patterned vascular networks for perfusable engineered three-dimensional tissues.* Nature materials, 2012. **11**(9): p. 768-774.
[38] Koolwijk, P., M. Van Erck, W. De Vree, M.A. Vermeer, H.A. Weich, R. Hanemaaijer, and V. Van Hinsbergh, *Cooperative effect of TNFalpha, bFGF, and VEGF on the formation of tubular structures of human microvascular endothelial cells in a fibrin matrix. Role of urokinase activity.* The Journal of cell biology, 1996. **132**(6): p. 1177-1188.
[39] Montesano, R., M.S. Pepper, and L. Orci, *Paracrine induction of angiogenesis in vitro by Swiss 3T3 fibroblasts.* Journal of cell science, 1993. **105**(4): p. 1013-1024.
[40] Raghavan, S., C.M. Nelson, J.D. Baranski, E. Lim, and C.S. Chen, *Geometrically controlled endothelial tubulogenesis in micropatterned gels.* Tissue Engineering Part A, 2010. **16**(7): p. 2255-2263.
[41] Yeon, J.H., H.R. Ryu, M. Chung, Q.P. Hu, and N.L. Jeon, *In vitro formation and characterization of a perfusable three-dimensional tubular capillary network in microfluidic devices.* Lab on a chip, 2012. **12**(16): p. 2815-2822.
[42] Kim, S., H. Lee, M. Chung, and N.L. Jeon, *Engineering of functional, perfusable 3D microvascular networks on a chip.* Lab on a Chip, 2013. **13**(8): p. 1489-1500.
[43] Hsu, Y.-H., M.L. Moya, C.C. Hughes, S.C. George, and A.P. Lee, *A microfluidic platform for generating large-scale nearly identical human microphysiological vascularized tissue arrays.* Lab on a Chip,

2013. **13**(15): p. 2990-2998.
[44] Lee, H., S. Kim, M. Chung, J.H. Kim, and N.L. Jeon, *A bioengineered array of 3D microvessels for vascular permeability assay.* Microvasc Res, 2014. **91**: p. 90-8.
[45] Huang, C.P., J. Lu, H. Seon, A.P. Lee, L.A. Flanagan, H.Y. Kim, A.J. Putnam, and N.L. Jeon, *Engineering microscale cellular niches for three-dimensional multicellular co-cultures.* Lab on a Chip, 2009. **9**(12): p. 1740-1748.
[46] Yuan, F., M. Leunig, D.A. Berk, and R.K. Jain, *Microvascular permeability of albumin, vascular surface area, and vascular volume measured in human adenocarcinoma LS174T using dorsal chamber in SCID mice.* Microvascular research, 1993. **45**(3): p. 269-289.
[47] Breslin, J.W., P.J. Pappas, J.J. Cerveira, R.W. Hobson, and W.N. Durán, *VEGF increases endothelial permeability by separate signaling pathways involving ERK-1/2 and nitric oxide.* American Journal of Physiology-Heart and Circulatory Physiology, 2003. **284**(1): p. H92-H100.
[48] Wang, L.-Y., D.-L. Zhang, J.-F. Zheng, Y. Zhang, Q.-D. Zhang, and W.-H. Liu, *Apelin-13 passes through the ADMA-damaged endothelial barrier and acts on vascular smooth muscle cells.* Peptides, 2011.
[49] He, P. and R.H. Adamson, *Visualization of Endothelial Clefts and Nuclei in Living Microvessels with Combined Reflectance and Fluorescence Confocal Microscopy.* Microcirculation, 1995. **2**(3): p. 267-276.
[50] Price, G.M., K.H. Wong, J.G. Truslow, A.D. Leung, C. Acharya, and J. Tien, *Effect of mechanical factors on the function of engineered human blood microvessels in microfluidic collagen gels.* Biomaterials, 2010. **31**(24): p. 6182-6189.
[51] Wu, M.H., E. Ustinova, and H.J. Granger, *Integrin binding to fibronectin and vitronectin maintains the barrier function of isolated porcine coronary venules.* The Journal of Physiology, 2001. **532**(3): p. 785-791.
[52] Brett, J., H. Gerlach, P. Nawroth, S. Steinberg, G. Godman, and D. Stern, *Tumor necrosis factor/cachectin increases permeability of endothelial cell monolayers by a mechanism involving regulatory G proteins.* The Journal of Experimental Medicine, 1989. **169**(6): p. 1977-1991.
[53] Horvath, C.J., T.J. Ferro, G. Jesmok, and A.B. Malik, *Recombinant tumor necrosis factor increases pulmonary vascular permeability*

independent of neutrophils. Proceedings of the National Academy of Sciences, 1988. **85**(23): p. 9219-9223.
[54] Stephens, K.E., A. Ishizaka, J.W. Larrick, and T.A. Raffin, *Tumor Necrosis Factor Causes Increased Pulmonary Permeability and Edema: Comparison to Septic Acute Lung Injury.* American Journal of Respiratory and Critical Care Medicine, 1988. **137**(6): p. 1364-1370.
[55] Burke-Gaffeyy, A. and A.K. Keenan, *Modulation of human endothelial cell permeability by combinations of the cytokines interleukin-1 α/β, tumor necrosis factor-α and interferon-γ.* Immunopharmacology, 1993. **25**(1): p. 1-9.
[56] Fu, B., R. Adamson, and F. Curry, *Test of a two-pathway model for small-solute exchange across the capillary wall.* American Journal of Physiology-Heart and Circulatory Physiology, 1998. **274**(6): p. H2062-H2073.
[57] Wong, K.H., J.M. Chan, R.D. Kamm, and J. Tien, *Microfluidic models of vascular functions.* Annual review of biomedical engineering, 2012. **14**: p. 205-230.
[58] Flament, J., F. Geffroy, C. Medina, C. Robic, J.-F. Mayer, S. Mériaux, J. Valette, P. Robert, M. Port, D. Le Bihan, F. Lethimonnier, and F. Boumezbeur, *In vivo CEST MR imaging of U87 mice brain tumor angiogenesis using targeted LipoCEST contrast agent at 7 T.* Magnetic Resonance in Medicine, 2013. **69**(1): p. 179-187.
[59] Curry, F. and W. Joyner, *Modulation of capillary permeability: methods and measurements in individually perfused mammalian and frog microvessels.* Endothelial Cells, 1988. **1**: p. 3-17.
[60] Turner, M.R. and T.L. Pallone, *Hydraulic and diffusional permeabilities of isolated outer medullary descending vasa recta from the rat.* American Journal of Physiology - Heart and Circulatory Physiology, 1997. **272**(1): p. H392-H400.
[61] Killackey, J., M. Johnston, and H. Movat, *Increased permeability of microcarrier-cultured endothelial monolayers in response to histamine and thrombin. A model for the in vitro study of increased vasopermeability.* The American journal of pathology, 1986. **122**(1): p. 50.
[62] Dvorak, H.F., L.F. Brown, M. Detmar, and A.M. Dvorak, *Vascular permeability factor/vascular endothelial growth factor, microvascular hyperpermeability, and angiogenesis.* The American journal of pathology, 1995. **146**(5): p. 1029.
[63] Carmeliet, P. and R.K. Jain, *Principles and mechanisms of vessel*

normalization for cancer and other angiogenic diseases. Nature Reviews Drug Discovery, 2011. **10**(6): p. 417-427.

[64] Dings, R.P., M. Loren, H. Heun, E. McNiel, A.W. Griffioen, K.H. Mayo, and R.J. Griffin, *Scheduling of radiation with angiogenesis inhibitors anginex and Avastin improves therapeutic outcome via vessel normalization.* Clinical cancer research, 2007. **13**(11): p. 3395-3402.

[65] Jain, R.K., *Normalization of tumor vasculature: an emerging concept in antiangiogenic therapy.* Science, 2005. **307**(5706): p. 58-62.

[66] Wang, W., W.L. Dentler, and R.T. Borchardt, *VEGF increases BMEC monolayer permeability by affecting occludin expression and tight junction assembly.* American Journal of Physiology-Heart and Circulatory Physiology, 2001. **280**(1): p. H434-H440.

[67] Pechman, K.R., D.L. Donohoe, D.P. Bedekar, S.N. Kurpad, R.G. Hoffmann, and K.M. Schmainda, *Characterization of bevacizumab dose response relationship in U87 brain tumors using magnetic resonance imaging measures of enhancing tumor volume and relative cerebral blood volume.* Journal of neuro-oncology, 2011. **105**(2): p. 233-239.

[68] Zen, K., D.-Q. Liu, Y.-L. Guo, C. Wang, J. Shan, M. Fang, C.-Y. Zhang, and Y. Liu, *CD44v4 is a major E-selectin ligand that mediates breast cancer cell transendothelial migration.* PloS one, 2008. **3**(3): p. e1826.

[69] Jöhrer, K., K. Janke, J. Krugmann, M. Fiegl, and R. Greil, *Transendothelial migration of myeloma cells is increased by tumor necrosis factor (TNF)-α via TNF receptor 2 and autocrine up-regulation of MCP-1.* Clinical cancer research, 2004. **10**(6): p. 1901-1910.

[70] Liang, M., P. Zhang, and J. Fu, *Up-regulation of LOX-1 expression by TNF-α promotes trans-endothelial migration of MDA-MB-231 breast cancer cells.* Cancer letters, 2007. **258**(1): p. 31-37.

[71] Zervantonakis, I.K., S.K. Hughes-Alford, J.L. Charest, J.S. Condeelis, F.B. Gertler, and R.D. Kamm, *Three-dimensional microfluidic model for tumor cell intravasation and endothelial barrier function.* Proc Natl Acad Sci U S A, 2012. **109**(34): p. 13515-20.

국문초록

구조적으로 정렬된 혈관 모사를 통한 정량적인 분석을 위한 미세유체소자 개발

이 현 재

서울대학교 대학원 기계전공

본 연구는 혈관 생물학 관련 모델을 만들기 위하여 구조적으로 정렬된 혈관을 생성하는 두 가지의 미세유체소자를 제시한다. 혈관 투과성 시험을 위하여, 여러 개의 관류 가능한 삼차원 미세혈관을 만들 수 있는 미세유체소자 구조를 설계 하였다. 본 플랫폼에서 형성된 미세혈관은 자연혈관신생형성 과정을 통하여 만들어 졌으며, 혈관 투과성 계수를 측정한 뒤 체내 혈관과의 비교를 통하여 적절한 수준의 장벽 특성을 지님을 확인하였다. 혈관 투과성의 변화 인자에 따른 투과성의 변화 양상 및 암 혈관 투과성 또한 재현하였다.

암 신생혈관형성 및 침윤 모델을 위하여, 비어있는 혈관 외 기질을 가지는 관류가능한 삼차원 미세혈관을 만들 수 있는 미세유체소자를 설계하였다. 암 신생혈관형성 시험을 위하여, U87MG 암 세포주를 혈관 외 기질에 주입하였다. 3일 후에 암 신생혈관형성과정에 따른 혈관이 보였으며, anti-VEGF 인자인 bevacizumab에 의하여 신생혈관형성을 상쇄하는 과정 또한 모사하였다. 암 침윤 모델을 위하여, MDA-MB-231 암 세포주를 혈관 외 기질에 주입하였으며 이들의 이동과정을 관찰하였다. TNF-α 처리를 통하여 혈관 장벽의 파괴를 확인하였으며, 이를 통하여 암 세포의 침윤 정도가 증가함을 확인하였다.

본 모델들은 암 세포 및 면역 세포의 혈관 투과 과정, 혈류에 따른 혈관 내피 세포의 반응 양상 등에 활용될 수 있다. 본 모델들의 높은 수준의 신뢰성 및 구조의 신축성은 추후 혈관 생물학 실험 및 약물 개발에 있어 다방면으로 활용될 것으로 전망된다.

주요어: 미세유체소자; 혈관신생형성; 혈관투과성; 관류가능한 미세혈관; 암전이; 조직공학

학번: 2012-30735